Evaluation of Direct FID-Based Dielectric Parameter Retrieval in MRI

Generalized Signal Models

Georgios Hadjigeorgiou

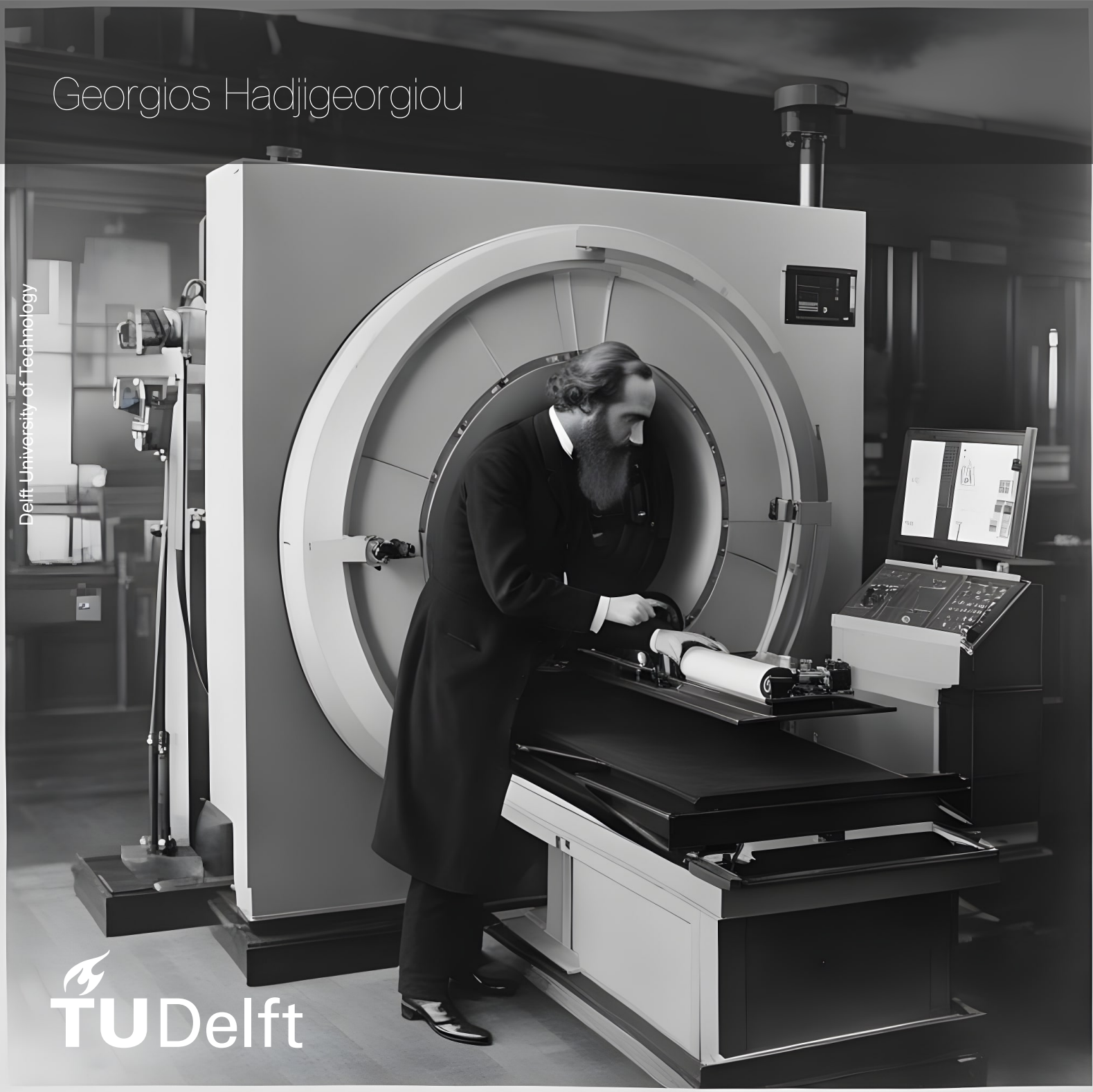

Delft University of Technology

TU Delft

Evaluation of Direct FID-Based Dielectric Parameter Retrieval in MRI

Generalized Signal Models

by

Georgios Hadjigeorgiou

to obtain the degree of Master of Science
at the Delft University of Technology,
to be defended publicly on Monday December 11, 2023 at 01:30 PM.

Student number:	4554956	
Project duration:	September 1, 2023 – December 11, 2024	
Thesis committee:	dr. ir. R. F. Remis,	TU Delft, supervisor
	dr. I. Costa,	TU Delft
	prof. dr. ir. C.A.T van den Berg, UMC Utrecht	
	dr. S. Mandija, UMC Utrecht	

This thesis is confidential and cannot be made public until December 31, 2024.

Cover:	AI Generated image from Dall-2 OpenAI, ”Maxwell operating an MRI machine”
Style:	TU Delft Report Style, with modifications by Daan Zwaneveld

An electronic version of this thesis is available at `http://repository.tudelft.nl/`.

TU Delft

Preface

Throughout my life and until this moment, I have had two interests that keep motivating me, technology and music. I have always perceived technology as a means to improve the quality of life and understand more about humans. During my bachelor's, I had the chance to explore various aspects of Electrical Engineering, but the one that really triggered my interest was medical imaging. I still find it very fascinating how much effort we put into understanding the whole universe and, at the same time, the same amount of effort we put into understanding the human body and how brains work.

Improving medical imaging techniques and building more sophisticated MRI machines are key factors in getting faster and more reliable diagnoses, thus improving people's quality of life and understanding more about the human body.

With this graduation project, my personal goal was to challenge myself and try to validate a new model that seems to be a solution for issues that modern high-field MRI machines exhibit. A very ambitious goal that made me understand more about MR imaging, challenged me to try to understand and explain certain phenomena, and allowed me to see the whole cycle of research and experiment.

I would like to first thank my supervisor at TU Delft dr. ir Rob Remis, for giving me the opportunity to work on this project and for his help and guidance. Moreover, I would like to thank Prof. dr. ir. Nico van den Berg and dr. Stefano Mandija from UMC Utrecht for their support in the experiment, their feedback and guidance on this project. I wouldn't have had the chance to run this experiment without you.

This graduation project closes a chapter of my life as this is the end of my university life. I couldn't be more grateful for having the chance to study at TU Delft, and spending one-third of my life in The Netherlands in a few years from now. All the memories, the people I met, and the experiences here have definitely changed me as a person, and I will always recall and share these memories in the future.

I would like to thank my family for their support and unconditional love throughout all these years. My friends and my study buddies, for the endless library studying hours and thousands of coffees we had together, and all the loved ones who have made this journey more pleasant. Without you, I am sure I wouldn't be able to make it so far.

Lastly, I hope that you, the reader, can be inspired by this report and help improve medical technology.

Georgios Hadjigeorgiou
Delft, December 2023

Summary

This thesis research focuses on MRI technology and more specifically the evaluation of the generalized signal model (full-wave signal). The research aims to investigate how dielectric properties influence the magnetic fields in MRI scans, by using a more complex signal model that takes into account scattered fields caused by dielectric properties of human tissue. Optimizing the Signal-to-Noise ratio (SNR) has been a main research focus since the invention of MRI machines. Higher-quality images, result in better diagnosis and therefore help the investigations of patient conditions. One way to improve the SNR is to operate MRIs in higher frequencies. Operating an MRI in higher frequencies, affects the measured signal at the receiving coil, as dielectric properties of biological tissue, induce currents due to magnetization. By having a full wave signal model, one can model the effect of the dielectric properties and thus take them into account when reconstructing an MRI image. The first step was to investigate whether a magnetic dipole can be simulated as a single emitting loop. The results from the simulation and the analytical solution have been compared. There's a high correlation between the two and thus it is concluded that it can be used. Using a single emitting loop, the effect of varying conductivity was simulated for a dielectric sphere placed in free space, with the single emitting loop submerged into the solution. The simulations showed that by increasing the conductivity, the measured voltage at the receiver coil reduces. Note that this simulation was performed twice, for relative permittivity values $\epsilon_r = 1$ and $\epsilon_r = 80$. The reason for choosing these two values was to first eliminate the effect of relative permittivity $\epsilon_r = 1$ and to simulate a water-based solution $\epsilon_r = 80$. Simulations verified that for $\epsilon_r = 1$, the measured voltage at the receiver location is lower than $\epsilon_r = 80$. After verifying the full-wave model and observing the effect of varying the electrical conductivity, two more simulations were performed to prepare for the experiment. In the first simulation, instead of a single loop, a series of loops was used to simulate the beam excitation of an MRI. As it is shown in the results, there is not a linear correlation between increasing the conductivity and the induced voltage at the receiver coil. Secondly, the experimental setup was simulated. In addition to the previous simulation, a plastic layer was added to the outside of the ball, to model the plastic sphere used during the experiment. In chapter 4, the results of the experiment are introduced. The results from the experiment could not justify the simulations due to reasons that are explained in the conclusions.

Contents

1

Introduction

Since the invention of Magnetic Resonance Imaging (MRI), researchers have aimed to improve the resulting image's resolution and quality. Moreover, MRI has helped medical doctors and researchers use this non-invasive imaging method to discover, diagnose, and guide treatment by using better-quality images and new image modalities. These improvements help to better investigate a patient's condition and allow us to have a more solid diagnosis. Hill and Richards [1] first explored ways to optimize the Signal-To-Noise Ratio (SNR) and provided ways to optimize it. For a Low and Medium-frequency MRI, SNR can be optimized with several techniques discussed later in this report. However, the need for higher SNR and better quality images pushed the MRI fields to higher frequencies and field strengths [2]. The advantage of using High-Field (HF)MRI is the resulting high SNR, higher sensitivity to Blood-oxygenation-level-dependent (BOLD) signals, and higher spatial resolution in the resulting anatomical images. The influence of the biological tissue on the measured signal at the receiver coil has always been at the center of research as it affects the sensitivity of the antenna [3]. Due to pushing the field to higher frequencies, RF coil design is becoming more challenging as the received signal is more sensitive to the dielectric properties of the tissue [3]. This is caused by the induced currents on biological tissue caused by magnetization, and nevertheless, in most of the current research, this phenomenon is neglected, as stated in [3]. This thesis report aims to investigate MRI signal models. It aims to validate our current understanding of how dielectric properties affect the signal measured by an MRI machine and introduce results that can potentially revolutionize MRI imaging.

This chapter provides a brief historical overview of MRI technology and highlights the importance of this research. Moreover, it introduces the challenges that we face with modern HF-MRIs and explains the importance of a new more complex generalized signal model.

Chapter two introduces the tomography roots, and categorizes the different imaging techniques while emphasizing the MRI's unique position. It provides a solid overview of MRI's fundamental and system-level principles, starting from nuclear resonance all the way to image reconstruction techniques.

Chapter three deep dives into the core of the thesis research. In this chapter the examination of the influence of dielectric properties on magnetic fields is conducted. By performing analytical studies and simulations, it aims to explore the complexities introduced by varying conductivity on a dielectric medium and the influence of relative permittivity.

In the fourth chapter, the aim is to validate this research with empirical evidence. The details of the conducted experiment are provided. This experiment aimed to validate the proposed generalized signal model. The employed methodology is explained, and the encountered challenges, the insights, and the results are presented.

To summarize, the research questions of this thesis research are,

- *Do the dielectric properties of tissues affect the received MRI signal?*
- *How do the dielectric properties alter the received signal?*
- *How does the excitation sequence affect the result for different dielectric properties?*
- *How does the generalized signal model compare to the standard model?*
- *Does the generalized signal model capture the effect of the dielectric properties for a sample undergoing an MRI scanning?*

2

Background

Tomography has always been a medical imaging field that has grown constantly since its invention. Creating images of the internal body with non-invasive methods is still the major benefit of biomedical imaging methods that are being used in clinical applications. Tomography can be divided into three categories, $emission$ tomography, $transmission$ tomography, and $diffraction$ tomography. CT and X-Ray imaging, belongs to transmission tomography, as the attenuation of high-energy particle beams transmitted through the body is measured and an image is formed. Both modalities involve ionizing radiation which in large quantities is known to be harmful to the human body. Diffraction tomography uses wavelengths on the same order of magnitude as the imaging body. The reconstruction of the body is based on measurements of the diffraction of the signal due to the body. MRI, similar to Positron Emission Tomography (PET) and Single-Photon Emission Computerized Tomography (SPECT) belongs to emission tomography. In contrast to PET and SPECT, MRI does not require the injection of any radioactive isotope into the object/body for a signal to be measured. MRI is the pinnacle when it comes to non-invasive, ionizing radiation-free, imaging techniques. In short, MRI, as a tomographic imaging modality, constructs an image of the internal physical characteristics of a body or an object, based on the received/measured signals of the nuclei of the body, at resonance frequencies. The resulting pixels of an MRI image are constructed based on the nuclear spin density ρ, the spin-lattice relaxation time T_1, and the spin-spin relaxation time T_2 and based on molecular diffusion (thermal motion) and perfusion. To enhance or suppress any of the aforementioned phenomena one can tune an MRI during the scanning or development stage by tuning several parameters. Those are echo time T_E, repetition time T_R, and flip angle α, among others. Based on the parameters, the resulting image taken from an MRI machine of an object/body may differ. For example in Figure 2.1, we can see that for the same head, different parameters and/or reconstruct methods result in a different, in terms of contrast, image.

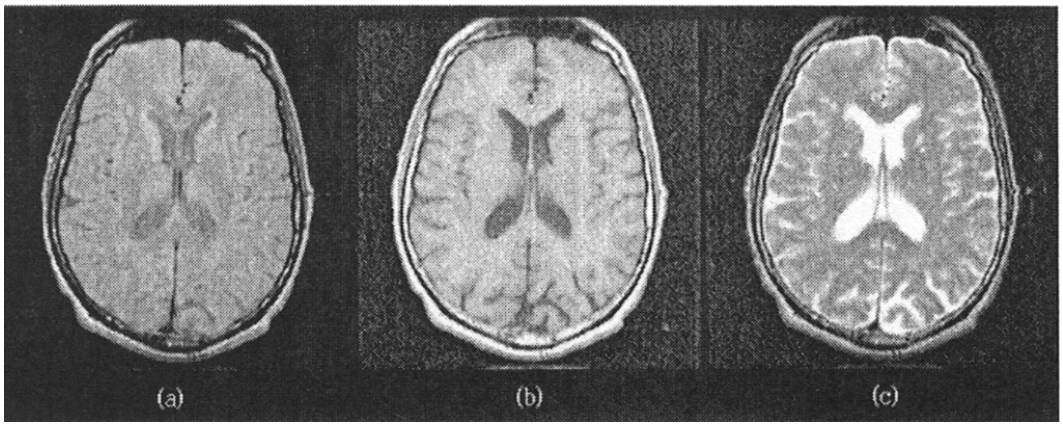

Figure 2.1: Cross-Section head image obtained using (a) Spin-density contrast ($T_E = 17ms$, $T_R = 2000ms$), (b) $T_1 weighted contrast$($T_E = 18ms$, $T_R = 400ms$) and (c) is $T_2 weighted contrast$($T_E = 80ms$, $T_R = 2500ms$), image source: [4]

2.1. Brief Introduction to MRI

Before diving into the mathematical models of MRI, there will be a brief introduction to MRI at a system level. In general, an MRI consists of 3 main components, the Main magnet, a Gradient system, and an RF system. The following three subsections explain the primary use and technology for each of the three systems.

2.1.1. Main magnet

The main magnet is used in an MRI to create a strong and uniform magnetic field B_0 that polarizes the spin of the nuclei within the body [4]. Depending on the strength, the main magnet can be a permanent magnet, resistive magnet, or superconducting magnet [4]. The decision on the B_0 field depends on the application. For example, recent advances in low-field MRI require a low B_0 field due to cost and clinical factors. Suppose a medical doctor wants, for example, to use an MRI during surgery. In that case, the doctor has to look into low-field solutions, as strong magnetic fields may affect the operation of other machines or tools used during the surgery. On the other hand, by having a high B_0 field, one can get high spectral-resolution images, as the higher the B_0, the higher the resulting Signal-To-Noise Ratio (SNR), as will be discussed later in this chapter. This, of course, comes with the cost of Rf-penetration problems and an expensive overall system. The field's homogeneity is the primary design problem regarding B_0 magnets. Homogeneity can be calculated by

$$Homogeneity = \frac{B_{0,max} - B_{0,min}}{B_{0,average}} \tag{2.1}$$

which is the maximum deviation of the field over the entire scanning body/object. For an acceptable image quality of a human body, it is required to have 10-50 parts-per-million (ppm) over a 30-50 cm spherical volume diameter according to [4]. In reality, no magnet can produce such a homogeneous magnetic field, thus, a secondary coil must compensate for the inhomogeneity [4]. These secondary coils are called shim coils, bringing the B_0 field to the desired homogeneity.

2.1.2. Gradient coil

As explained in chapter 1.2.2 in [4], gradient coils produce non-uniform, time-varying magnetic fields and are very important in MRI, as they are required for signal localization. The essential characteristics of a gradient system are the maximum gradient strength and the maximum gradient strength rate. A commonly used maximum gradient strength is about 10 mT/m [4]. Rise time is the time required to achieve this maximum strength. Generally speaking, the smaller this time, the better the system is. This is because the higher the rise time the bigger the resulting anatomical slice will be and thus lower resolution. According to [4], in clinical MRI, such a time is around 1 ms from 0 to 10 mT/m.

2.1.3. The RF System

The RF system is made up first of a coil responsible for producing a time-varying (rotating) magnetic field (B_1 field) that excites the atoms and, secondly, by a receiver coil that converts the relaxation of atoms, during their return to equilibrium, into electrical signals. Note that these two coils are not necessarily two different coils. Some MRIs use transceivers, where the same coil is used for both transmitting and receiving the signals. The name RF system is used because these coils resonate at radio frequencies that excite and measure nuclear spin. RF coils create a uniform B_1 field as uniform as possible and exhibit high sensitivity for signal detection. Different RF coils are used to achieve both, especially the latter, based on which part of a body is being imaged. According to [4], a birdcage coil is used when scanning the head, as it provides the highest homogeneity. One can use a cylindrical coil for other body parts, such as legs.

2.2. Standard MRI Signal Model

The standard MRI signal model is currently being used in practice. All the MRI machines from Low to High fields reconstruct images from measured signals based on this model. The following section is divided into four subsections. The first subsection introduces MRI image reconstruction at an abstract level. The latter three subsections explain how starting from the magnetization of a single nucleus, we end up receiving a signal on an MRI coil and, lastly, how the image is reconstructed.

2.2.1. MRI Image Reconstruction Principles

The following subsections explain how the MRI image reconstruction works. Starting from the microscopic magnetic moment to the resulting image. At first, the data has to be collected, and then an image has to be constructed based on this data. The first part of collecting the data is called $imaging\ equation$*, and the construction of the image is called* $image\ reconstruction\ equation$*, as explained in [4]. The first term is referred to what mathematically is called* $forward\ problem$*, and the latter is called* $inverse\ problem$*. In [4], to give an initial idea of how one can get from MRI signal to 3D or 4D images, the following sequence is introduced*

$$\vec{\mu} \rightarrow \vec{M} \rightarrow \vec{M_{xy}} \rightarrow S(t) \rightarrow S(\vec{k}) \rightarrow I(\vec{x}) \tag{2.2}$$

where, $\vec{\mu}$ *is microscopic magnetic moments in a body/object,* $\vec{M}$ *is a bulk magnetization,* $\vec{M_{xy}}$ *is the transverse magnetization,* $S(t)$ *is the electrical signal,* $S(\vec{k})$ *is a k-space signal and lastly* $I(\vec{x})$ *the resulting image. Each of these transformations is related to the main MRI system components discussed before (the MRI model currently used in practice). As explained in [4], the transformation* $\vec{\mu} \rightarrow \vec{M}$ *is related to the main magnetic field* B_0 *and is achieved by exposing the Hydrogen nuclei to* B_0*. Moreover,* $\vec{M} \rightarrow \vec{M_{xy}}$ *is achieved by the RF excitation, and* $\vec{M_{xy}} \rightarrow S(t)$ *is measuring a signal at the receiving coils after being excited by the RF system. Faraday's Law of Induction governs it. The last part of these transformations is the main topic of this research, that is, the* $S(\vec{k}) \rightarrow I(\vec{x})$*. Based on the image reconstruction model, one can get an image from k-space domain measurements. In the following parts of this chapter, the current ways of reconstructing an image will be introduced, and at the end, the new generalized signal model. However, before discussing reconstruction, it's important to review the earlier steps, especially the transition from* $\vec{\mu} \rightarrow S(\vec{k})$*, as it will be more clear mathematically how* $S(\vec{k})$ *is being generated.*

2.2.2. Underlying Physics for $\vec{\mu} \rightarrow \vec{M}$

In chapter 3.1.1 in [4], it is explained how the nuclear magnetic moments μ *come from the atom's nuclear spin and that a nucleus (filled with protons) has electrons spinning around it, and the whole atom spins around its axis. Furthermore, any spinning electrically charged body field produces a magnetic field around itself with a magnetic moment vector* $\vec{J}$ *related to the angular magnetic moment* $\vec{\mu}$ *by*

$$\vec{\mu} = \gamma \vec{J} \tag{2.3}$$

where γ *is the gyromagnetic ratio and varies based on the atom's nucleus. As stated in [4], atoms within a body have random magnetic moments and, summed up, give zero. To enable the magnetization of several atoms, one has to expose these atoms to a magnetic field*

$$\vec{B_0} = B_0 \vec{k} \tag{2.4}$$

as discussed earlier. Something crucial in signal detection and the basis of MR methods is that the magnetic moment aligns only partially with $\vec{k}$ *[4]. That is because an atom has discrete orientations based on quantum theory. Using Figure 3.3, page 62 in [4], it can be seen that if the direction of the applied* B_0 *field is oriented towards the z-axis, then the resulting moment* $\vec{\mu}$ *can be depicted in Figure 2.2.*

The relation between $\vec{B_0}$ *and* $\vec{\mu}$ *can be derived by classical mechanics and is governed by*

$$\frac{d\vec{J}}{dt} = \vec{\mu} \times B_0 \vec{k}, \tag{2.5}$$

and by using equation 2.3

$$\frac{d\vec{\mu}}{dt} = \gamma \vec{J} \times B_0 \vec{k}, \tag{2.6}$$

The solution to equation 2.6, as stated in [4], can be expressed by

$$\begin{cases} \mu_{xy}(t) = \mu_{xy}(0) e^{-i\gamma B_0 t}, \\ \mu_z(t) = \mu_z(0) \end{cases} \tag{2.7}$$

The angular frequency

$$\omega_0 = \gamma B_0, \tag{2.8}$$

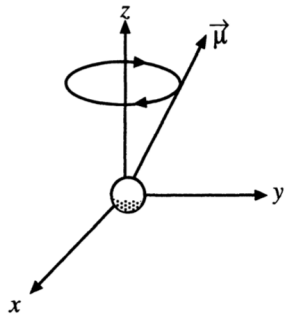

Figure 2.2: Magnetic moment orientation of an atom excited in a B0 field towards z-direction, image source: [4]

is called the Larmor frequency. By relating the B_0 field strength with the angular frequency, one can choose the natural resonance frequency of the spin system. Simply put, one can select which atoms within the body will be "scanned." Based on the initial position of the atom, they could end up being parallel or antiparallel. Parallel are the atoms whose z component is parallel to that of B_0, and antiparallel are those that are antiparallel to it.

When it comes to the bulk magnetization of a certain area within the object/body, one has to sum up the magnetic moments of all nuclei within that object, expressed by

$$\vec{M} = \sum_{n=1}^{N_s} \vec{\mu_n} \tag{2.9}$$

As mentioned in [4],to be able to detect $\vec{M}$ by the RF receiving coils, three concerns have to be addressed:

- *The portion of magnetization on the x,y plane (μ_{xy}) has to be manipulated to measure the magnetic field in the closed contour at the x,y plane, as it is random.*
- *Signal has to be strong enough to be detected by the receiving coil*
- *Parallel and antiparallel nuclei can not be equal*

The first two requirements can be met by properly designing the RF-excitation coil. Quantum mechanics meets the third requirement, which is beyond this research's scope. The number of antiparallel nuclei is slightly more than the rest because it is more likely for an atom to take the lower-energy state, for higher stability, than the higher-energy state while being excited by B_0. Now the remaining question is how B_1 is used to achieve the desired goal of measuring the total Magnetization $\vec{M}$.

2.2.3. The Bloch Equation - $\vec{M} \rightarrow \vec{M_{xy}} \rightarrow S(t)$

Up to now, the analysis was based solely on the presence of a B_0 field and just introduced the basics of an atom's behavior in the presence of static magnetic fields. With the introduction of $B_1(t)$, a time-varying magnetic field, the Bloch equation that governs MRI's Magnetization $\vec{M}$ is expressed by

$$\frac{d\vec{M}}{dt} = \gamma \vec{M} x \vec{B} - \frac{M_x \vec{i} + M_y \vec{j}}{T_2} - \frac{(M_z - M_z^0)\vec{k}}{T_1} \tag{2.10}$$

as explained in [4]. The RF pulse produced by the RF excitation coil introduced before manages to perturb the spin system from its thermal equilibrium state. According to the laws of thermodynamics, the system will return to its initial state when the external force is removed. This procedure can be divided into three constitutional events. The first is the so-called $free\ precision$ and is marked by the precession of $\vec{M}$ and B_0 field. The next is the so-called $longitudinal\ relaxation$ characterized by the destruction of the M_z field component. Lastly, the $transverse\ relaxation$ is characterized by the destruction of the M_{xy}. To measure the received signal we can use Faraday's Law. The induced voltage V(t) across the receiver coil is expressed by

$$V(t) = -\frac{\partial \Phi(t)}{\partial t} = -\frac{\partial}{\partial t}\int_{object} \vec{B_r}(r).M(\vec{r},t)\,dr \tag{2.11}$$

In [4], it is mentioned that by decomposing B and M into Cartesian components and by dropping the M_z component due to its slow varying nature we get,

$$V(t) = -\int_{object} [B_{r,x}(r)\frac{\partial M_x(r,t)}{\partial t} + B_{r,y}(r)\frac{\partial M_y(r,t)}{\partial t}]\,dr \tag{2.12}$$

In equation 2.12, it is clear why the coil's signal depends only on the transverse magnetization (M_x and M_y). By applying multiple techniques and calculations in [4] they end up with the expression

$$S(t) = \int_{object} M_{xy}(r,0)e^{-i\gamma\Delta B(r)t}\,dr \tag{2.13}$$

Observe that the signal S(t) is the Fourier transform of the signal at a location r. This is powerful as one can sample in the Fourier space domain and then apply the Inverse Fourier transform to get the final image, by measuring a signal in the time domain.

2.2.4. The MRI Signal Model - $S(t) \rightarrow S(k) \rightarrow I(x)$

We can formulate the problem of reconstructing a function $I(r)$ from its Fourier series samples as

$$S(k_n) = \int I(r)e^{-i2\pi k_n.r}dr \tag{2.14}$$

where k_n is within the object k-space domain. Although this seems straightforward, the reality is far from that. Usually, there are multiple solutions to this inverse problem due to noise and undersampling of the data received. Moreover, S^{-1} is unstable and non-invertible. There are two ways to reconstruct the image based on the way data was sampled. The two sampling methods can be observed in Figure 2.3 from chapter 6.2.2 in [4].

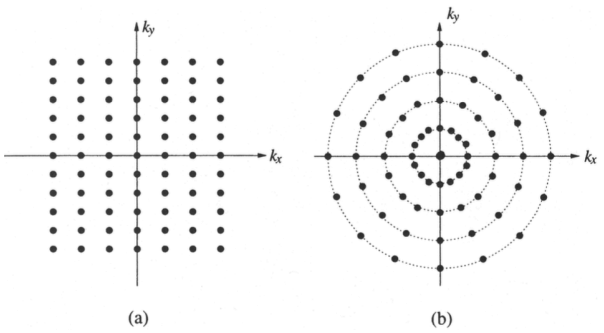

Figure 2.3: Two basic k-space coverage used in MRI, image source:
[4]

If the data is sampled as in 2.3(a), then Direct FFT Reconstruction is used. If the data is sampled as in 2.3(b), then Inverse Radon Transform is used (Backprojection Reconstruction) as explained in [4].

As it is clearer now, the standard Signal Model explained in this section is solely based on the excitation of the nuclei. During the image reconstruction, from the measured signals, the dielectric properties of the excited body/object are not taken into account. For this reason, a new generalized model was introduced in [3], where dielectric properties are considered.

2.3. Generalized MRI Signal Model

In [3], a new MRI full-wave signal model was created, based on scattering fields where the object present in the MRI experiment is taken into account by modeling it as an electric scattering source.

2.3.1. Scattering and Background Magnetic fields

In [3], at first the formulation of the background field is calculated using Maxwell's equations

$$-\nabla \times \hat{\mathbf{H}}^{b} + \sigma_b \hat{\mathbf{E}}^{b} + s\epsilon_b \hat{\mathbf{E}}^{b} = 0 \tag{2.15}$$

and

$$-\nabla \times \hat{\mathbf{E}}^{b} + s\mu_b \hat{\mathbf{H}}^{b} + s = -\hat{\mathbf{K}} \tag{2.16}$$

where H is the magnetic field and superscript b denotes the background magnetic field. Similarly, E is the electric field, and finally, K is the Laplace transform, of $\mu_0 \delta_t M$, where $\mathbf{M}(\mathbf{x}, t)$ is the time-varying magnetization within the domain of excitation $\mathbb{D}_{ex}$.

More explicitly, the magnetic field in the background can be expressed by

$$\hat{\mathbf{H}}^{b}(\mathbf{x}, s) = \int_{\mathbf{x}' \in \mathbb{D}_{ex}} \hat{\mathbf{G}}^{HK}(\mathbf{x}, \mathbf{x}', s).\hat{\mathbf{K}}(\mathbf{x}', s)dV \tag{2.17}$$

and similarly, the electric field by

$$\hat{\mathbf{E}}^{b}(\mathbf{x}, s) = \int_{\mathbf{x}' \in \mathbb{D}_{ex}} \hat{\mathbf{G}}^{EK}(\mathbf{x}, \mathbf{x}', s).\hat{\mathbf{K}}(\mathbf{x}', s)dV \tag{2.18}$$

where $\hat{G}$'s are the corresponding Green's tensors for the magnetic current to the magnetic field and magnetic current to the electric field.

The scattered field satisfies Maxwell's equations too. Thus it can be expressed by

$$-\nabla \times \hat{\mathbf{H}}^{sc} + \sigma_b \hat{\mathbf{E}}^{sc} + s\epsilon_b \hat{\mathbf{E}}^{b} = -\hat{\mathbf{J}}^{sc} \tag{2.19}$$

and

$$-\nabla \times \hat{\mathbf{E}}^{b} + s\mu_b \hat{\mathbf{H}}^{b} + s = -\hat{\mathbf{K}} \tag{2.20}$$

where

$$\hat{\mathbf{J}}^{sc}(\mathbf{x}, s) = \hat{\sigma}(\mathbf{x}) - \sigma_b(\mathbf{x}) + s[\hat{\epsilon}(\mathbf{x}) - \epsilon_b(\mathbf{x})]\hat{\mathbf{E}}(\mathbf{x}, s) \tag{2.21}$$

and where $x \in \mathbb{D}_{obj}$, in the domain of the object, $\hat{\sigma}(\mathbf{x})$ is the conductivity of the object and $\hat{\epsilon}(\mathbf{x})$ its permittivity as introduced in [3]. Similarly $\hat{\sigma}_b(\mathbf{x})$ and $\hat{\epsilon}_b(\mathbf{x})$ are background's conductivity and permittivity.

The integral expression for the scattered field of the Magnetic and Electric fields are given by

$$\hat{\mathbf{H}}^{sc}(\mathbf{x}, s) = \int_{\mathbf{x}' \in \mathbb{D}_{ex}} \hat{\mathbf{G}}^{HJ}(\mathbf{x}, \mathbf{x}', s).\hat{\mathbf{J}}^{sc}(\mathbf{x}', s)dV \tag{2.22}$$

and

$$\hat{\mathbf{E}}^{sc}(\mathbf{x}, s) = \int_{\mathbf{x}' \in \mathbb{D}_{ex}} \hat{\mathbf{G}}^{EJ}(\mathbf{x}, \mathbf{x}', s).\hat{\mathbf{J}}^{sc}(\mathbf{x}', s)dV \tag{2.23}$$

2.3.2. Full-wave Signal Model

By having the background and scattered fields introduced, the generalized signal model (full-wave signal model) developed in [3] can be expressed by

$$\hat{d}_h(s) = \int_{\mathbf{x} \in \mathbb{D}_{ant}}' \hat{\mathbf{m}}_h(\mathbf{x}, s) \cdot \int_{\mathbf{x}' \in \mathbb{D}_{ex}} \hat{\mathbf{G}}^{HK}(\mathbf{x}, \mathbf{x}', s) \cdot \hat{\mathbf{K}}(\mathbf{x}', s)dVdV + \int_{\mathbf{x} \in \mathbb{D}_{ant}}' \hat{\mathbf{m}}_h(\mathbf{x}, s) \cdot \int_{\mathbf{x}' \in \mathbb{D}_{obj}} \hat{\mathbf{G}}^{HJ}(\mathbf{x}, \mathbf{x}', s) \cdot \hat{\mathbf{J}}^{sc}(\mathbf{x}', s)dVdV \tag{2.24}$$

and

$$\hat{d}_e(s) = \int_{\mathbf{x} \in \mathbb{D}_{ant}}' \hat{\mathbf{m}}_e(\mathbf{x}, s) \cdot \int_{\mathbf{x}' \in \mathbb{D}_{ex}} \hat{\mathbf{G}}^{EK}(\mathbf{x}, \mathbf{x}', s) \cdot \hat{\mathbf{K}}(\mathbf{x}', s)dVdV + \int_{\mathbf{x} \in \mathbb{D}_{ant}}' \hat{\mathbf{m}}_e(\mathbf{x}, s) \cdot \int_{\mathbf{x}' \in \mathbb{D}_{obj}} \hat{\mathbf{G}}^{EJ}(\mathbf{x}, \mathbf{x}', s) \cdot \hat{\mathbf{J}}^{sc}(\mathbf{x}', s)dVdV \tag{2.25}$$

where $\hat{\mathbf{m}}_h(\mathbf{x}, s)$ and $\hat{\mathbf{m}}_e(\mathbf{x}, s)$ are vectorial functions, used to express the action of the receiver to the electromagnetic field inside the ball for the magnetic and electric field respectively. By rearranging the order of integration and using properties of Green's tensors such as reciprocity [3], the equation can be rewritten.

$$\hat{d}_h(s) = \int_{\mathbf{x}' \in \mathbb{D}_{\mathbf{ex}}}' \hat{\mathbf{K}}(\mathbf{x}', s) \cdot \hat{\mathbf{W}}_h^{mg}(\mathbf{x}', s) dV - \int_{\mathbf{x}' \in \mathbb{D}_{\mathbf{obj}}}' \hat{\mathbf{J}}^{sc}(\mathbf{x}', s) \cdot \hat{\mathbf{W}}_e^{mg}(\mathbf{x}', s) dV \tag{2.26}$$

and

$$\hat{d}_e(s) = -\int_{\mathbf{x}' \in \mathbb{D}_{\mathbf{ex}}}' \hat{\mathbf{K}}(\mathbf{x}', s) \cdot \hat{\mathbf{W}}_h^{el}(\mathbf{x}', s) dV + \int_{\mathbf{x}' \in \mathbb{D}_{\mathbf{obj}}}' \hat{\mathbf{J}}^{sc}(\mathbf{x}', s) \cdot \hat{\mathbf{W}}_e^{el}(\mathbf{x}', s) dV \tag{2.27}$$

where $\mathbf{W}_h^{mg}(\mathbf{x}', s)$, $\mathbf{W}_e^{mg}(\mathbf{x}', s)$ are the received fields for magnetic field measurement and $\mathbf{W}_h^{el}(\mathbf{x}', s)$, $\mathbf{W}_e^{el}(\mathbf{x}', s)$ are the received fields for electric field measurement.

Equations 2.27 and 2.26 are the full-wave signal models for measuring the electric and magnetic fields. The magnetic and scattering electric sources contribute to the measured signal. This model allows us to optimize the signal reception quality by using Green's tensors to tune the receiving antennas and coils.

2.4. Consequences of using the Standard Model

In the resulting images of high-field MRIs, signal loss (i.e. signal voids or artifacts) is often observed [5]. These artifacts are the result of waves interfering within the body due to scattering[5]. The MRI model can optimize the SNR resulting in the ultimate SNR, as will be further discussed. Still, it now enables us to solve the problem of the signal void, which is something, among others, that the generalized signal model aims to solve.

2.4.1. SNR optimization

Since the invention of Magnetic Resonance Imaging (MRI), researchers have aimed to improve the resulting image's Signal-to-Noise Ratio (SNR). As explained in [1], the theoretical limiting Signal-To-Noise Ratio (SNR) (the maximum achievable SNR) for a sample placed in a coil with a quality factor Q that resonates at the Larmor frequency ω_0, constant magnetic field (z-axis) B_0 and a rotating magnetic field B_1 is given by

$$\frac{V_s}{V_n} = K \frac{\eta Q^{1/2} \omega_0^{1/2} V_c^{1/2}}{(4kT\Delta f F)^{1/2}} 2\chi B_1, \tag{2.28}$$

where χ is the susceptibility, η is the filling factor of the receiver coil, ω_0 is the Larmor frequency, and V_c the coil volume.

In 1968 Hill and Richards [1] analyzed the numerous factors that affect the Signal-To-Noise Ratio (SNR) of a body placed in a magnetic resonance imaging machine. The first factor to be considered is field inhomogeneity. It is suggested that $T2$ time should be about $2/\gamma\Delta B$ where ΔB is the magnetic field inhomogeneity [1]. To observe the resonance line shape, the magnetic field inhomogeneity has to be smaller than the actual line width. In practice, to achieve field homogeneity to a certain level, the magnet's geometry and material must be selected carefully, and field-correcting coils must be used [1].

From equation 2.28, it is clear that quality factor Q can also affect the SNR [1]. In general, Q can be expressed as

$$Q = \frac{\omega E}{P}, \tag{2.29}$$

where ω is the angular frequency, E is the energy stored in the circuit, and P is the power dissipated in the circuit as explained in [1]. For a coil, as skin depth decreases ($\omega^1/2$ increases), power dissipation increases, and thus quality factor decreases. Moreover, it has to be noted that with higher frequencies, interwinding capacitance comes into play, resulting in dielectric losses on the coil [1]. By designing the coil's geometry so that its maximum Q is in the range of frequencies of operation, a high Q can be achieved [1].

Instead of increasing signal power, one can find ways to minimize noise power. Noise appears in many parts of the circuit, such as the microwave source, oscillators, receiver's noise, couplers, drift in D.C amplifiers, etc [1]. In particular, the resonant circuit is being affected by low-frequency variations because of mechanical and thermal effects [1]. Thus, these effects can be minimized by making a sturdy design and keeping the temperature as stable as possible. Another way to solve the low-frequency noise is to modulate the signals with a high-frequency signal [1]. In practice, the most widely used technique to modulate the signal is by applying sinusoidal field modulation [1]. In an ideal case scenario, the resulting signal would contain modulated signals at the chosen modulation frequency and its harmonics. However, in real-life scenarios, various mechanical or electronic components "respond" to the modulation frequency, producing additional signals [1].

In [6], there is a first attempt to quantify the power dissipation and phase shift of the magnetic field that penetrated biological tissue samples during NMR imaging experiments. Two models have been used, a planar and a cylindrical model. At first, it is shown that for a skin depth of 20 cm, there is a 37% attenuation in the amplitude of the signal compared to that on the skin surface at frequencies around $20MHz$. Furthermore, a phase shift of 80 was observed. It is concluded that the signal amplitude attenuation will produce shades in the NMR image and that the phase shifts will produce distortions. They conclude that the frequency of the magnetic field should be chosen wisely based on the material used in the NMR imaging machines.

Much research was conducted on calculating the ultimate-Signal-to-Noise Ratio on MRIs by optimizing the magnetic field. For example, in [7], the first proposal uses multiple antennas (antenna arrays) to receive a signal instead of one coil. By measuring the antenna's output voltage, one can calculate the optimal complex weights (amplitude and phase) for each antenna and then perform a weighted sum to get the resulting "optimal" field. With a quasi-static approximation, an infinite number of small loops, and zero distance between the antenna and the tissue, an 8% increase in SNR was achieved theoretically [7]. Furthermore, by assuming that the noise is non-white, one can use a matched filter for non-white noise to optimize the antenna weights. Another interesting finding is that for homogeneous muscle tissue and a frequency-independent magnetization, frequencies above $20MHz$ and small tissue-coil distance, the optimum SNR for the receiving antenna can be calculated [7].

Apart from coil design and magnetic field power dissipation, the tissue itself plays a significant role, according to [8]. SNR strongly depends on the geometry of the tissue but also on the physical properties such as electrical properties, dimensions, conductivity, etc. Moreover, parallel-image reconstruction affects the resulting SNR [8]. This paper finds the optimal amplitude and phase for RF shimming when a ball is placed in the MRI.

In [9], they have managed to model and calculate the uSNR for realistic body models by using the SNR equation from [8] and deriving it per unit of volume. In the end, they compared the results for different frequencies and conductivity values of a homogeneous sphere. In general, the uSNR of the realistic models was lower than a then homogeneous sphere. It has to be noted that the real head model was assumed to have isotropic electrical properties.

Multiple ways to optimize the SNR were introduced up to this point. However, even in the case of [8], the so-called realistic model of the head has isotropic electrical properties, which affect the resulting SNR. In [10], they tried to get the dielectric properties by evaluating the relaxation time $T1$ and, based on that, estimate the water content of the voxel to calculate the dielectric properties of a voxel. Each slice is made of several voxels, representing the intensity of the measured signal. This received intensity is linked to the relaxation times, which in sequence are linked to the water concentration in that specific area. By having the water concentration, one can use dielectric tissue models, for example, the one in [11].

2.4.2. Dielectric properties extraction

Extraction of electrical properties has been a topic of research since the early years of MRI [12]. This paper uses the received signal from the $B1$ field to estimate the properties. However, the results in [12], have considerable discrepancies when noise is added, and it concluded that this method is insensitive to dielectric properties when the thickness is less than 0.5 cm. The conductivity is less than 0.1 Sm^{-1}. Electrical properties tomography is based on [11]. It again utilizes the RF coil-induced $B1$ field to reconstruct the electrical properties and develop the electrical properties map. The benefit of this technique is that it is non-invasive and does not require the insertion of electrodes inside the body. However, this method requires manual tissue segmentation and can not be used with complicated

anatomical structures. A similar approach was followed in [13]; however, only the phase of $B1$ was used, resulting in not estimating permittivity as a cost for speeding up the computation process.

All the methods above rely heavily on the MRI reconstructed images to calculate dielectric properties. When the resulting images contain artifacts, which is something usual for HF and UltraHF MRIs, then the results are poor. The main question of this research is to evaluate and extend the research on the generalized signal model to investigate whether changes in the dielectric properties of the sample being scanned affect the received signal.

2.5. Generalized signal model formulated for FID Signals for a ball in space

In this section, the model is expressed for the case of a ball being excited by FID-based signals as derived in [3]. As will soon be apparent, the dielectric properties affect the resulting signal, which might indicate why the standard signal model gives artifacts in the resulting image. In the full-wave signal model, i.e., equations 2.27 and 2.26, both scattering and magnetization contribute to the measured signal. On the contrary, for the standard signal model, only magnetization contributes. Background medium, receiving coils, and antennas are all included in Green's tensors, and all can be used to optimize the receiving signal for certain applications [3]. These coils further optimize the resulting MRI image to exclude the "signal voids" in high-field MRI images. Moreover, the generalized signal model seems to be able to retrieve the body's dielectric properties [3]. Free Induction Decay signals are induced in an MRI coil after the excitation of the RF system. At first, the ball is assumed to lie in the free space. By making such an assumption, Green's tensors can be easily calculated [3]. Furthermore, it is assumed that the ball has homogeneous dielectric properties. Lastly, by having a sufficiently small radius of the ball, the total electric field due to a magnetization within the ball's domain can be derived explicitly as introduced in [3], and is given by

$$\hat{\mathbf{E}}(\mathbf{x}^{'},\mathbf{s}) = \hat{\mathbf{E}}^{\mathbf{b}}(\mathbf{x}^{'},s) - \hat{\chi}(\hat{\gamma}^2 - \nabla\nabla\cdot)\int_{\mathbf{x}\in\mathbb{D}_{\mathbf{obj}}} \hat{G}(\mathbf{x}-\mathbf{x}^{'},s)\hat{\mathbf{E}}(\mathbf{x}^{'},s)dV \tag{2.30}$$

where $\hat{\gamma} = s/c_0$ is the propagation coefficient of free space, $\hat{\chi} = \hat{\epsilon_r} - 1 + \hat{\sigma}/(s\epsilon_0)$ is the ball's contrast. Several conditions must be met to arrive at the desired models for a ball in free space. Moreover, in [3], by assuming quasi-static conditions that Born approximation holds, band limiting the magnetization around Larmor frequency and applying inverse Laplace transform to equations 2.27 and 2.26, then the model in time-domain turns into

$$d_h(t) = \mu_0\partial_t\mathbf{M}(t) * \int_{\mathbf{x}\in\mathbb{D}_{\mathbf{obj}}} \mathbf{S}^{mg}(\mathbf{x}^{'},t-\tau)dV \tag{2.31}$$

and

$$d_e(t) = -\mu_0\partial_t\mathbf{M}(t) * \int_{\mathbf{x}\in\mathbb{D}_{\mathbf{obj}}} \mathbf{S}^{el}(\mathbf{x}^{'},t-\tau)dV \tag{2.32}$$

where convolution is performed in the time domain and the sensitivity functions are given by

$$\mathbf{S}^{\mathbf{mg}}(\mathbf{x}^{'},t) = \frac{A}{4\pi|\mathbf{x}^{'}-\mathbf{x}_R|^3}\sum_{k=0}^{3}\tau^k\delta^{(k)}(t)\mathbf{r}_{\mathbf{k}}^{\mathbf{mg}} \tag{2.33}$$

and

$$\mathbf{S}^{\mathbf{el}}(\mathbf{x}^{'},t) = \frac{A}{4\pi|\mathbf{x}^{'}-\mathbf{x}_R|^3}\sum_{k=0}^{3}\tau^k\delta^{(k)}(t)\mathbf{r}_{\mathbf{k}}^{\mathbf{el}} \tag{2.34}$$

The expansion vectors and a more analytical derivation of this model can be found in [3].

2.5.1. Sensitivity of the generalized signal model

To evaluate the generalized signal model, it is wise to investigate what affects the measured signal. To have a successful evaluation, the generalized signal model has to be further simplified. Firstly, the travel time of the waves and the propagation effects are considered in equations 2.34 and 2.33. However, the

receiver (measuring coil) is located very close to the ball's surface, and thus the model can be further simplified [3]. The simplified models are given by

$$\begin{aligned}\hat{d}_h^{QS}(t) \approx \\ &\frac{\mu_0 A}{4\pi}[\partial_t \mathbf{M} \cdot \int_{\mathbf{x}' \in \mathbb{D}_{\mathbf{obj}}} \frac{\mathbf{p_1}}{|\mathbf{x}' - \mathbf{x_R}|^3} dV \\ &+ \frac{\sigma\mu_0}{3}\partial_t^2 \mathbf{M} \cdot \int_{\mathbf{x}' \in \mathbb{D}_{\mathbf{obj}}} \frac{[(\mathbf{x}' \cdot \nu)\mathbf{n} - (\mathbf{x}' \cdot \mathbf{n})\nu]}{|\mathbf{x}' - \mathbf{x_R}|^2} dV \\ &+ \frac{\epsilon_r - 1}{3}\frac{1}{c_0^2}\partial_t^3 \mathbf{M} \cdot \int_{\mathbf{x}' \in \mathbb{D}_{\mathbf{obj}}} \frac{[(\mathbf{x}' \cdot \nu)\mathbf{n} - (\mathbf{x}' \cdot \mathbf{n})\nu]}{|\mathbf{x}' - \mathbf{x_R}|^2} dV]\end{aligned} \tag{2.35}$$

and

$$\begin{aligned}\hat{d}_e^{QS}(t) \approx \\ &\frac{\mu_0 A}{4\pi}[\frac{\sigma}{3}\partial_t \mathbf{M} \cdot \int_{\mathbf{x}' \in \mathbb{D}_{\mathbf{obj}}} \frac{\mathbf{x}' \times \mathbf{p_1}}{|\mathbf{x}' - \mathbf{x_R}|^3} dV \\ &+ \frac{\epsilon_r - 1}{3}\partial_t^2 \mathbf{M} \cdot \int_{\mathbf{x}' \in \mathbb{D}_{\mathbf{obj}}} \frac{\mathbf{x}' \times \mathbf{p_1}}{|\mathbf{x}' - \mathbf{x_R}|^3} dV \\ &+ \epsilon_0 \partial_t^2 \mathbf{M} \cdot \int_{\mathbf{x}' \in \mathbb{D}_{\mathbf{obj}}} \frac{\nu \times \mathbf{n}}{|\mathbf{x}' - \mathbf{x_R}|^2} dV]\end{aligned} \tag{2.36}$$

where x_R is the barycenter of the receiver coil, $x^{'}$ is the integration point within the object, σ is object's conductivity, ϵ_r is the relative permittivity, $\mathbf{p_1} = 3\mathbf{n}((\mathbf{n} \cdot \nu) - \nu)$, ν is the receiver coil orientation unit vector, and n is the unit vector pointing from the receiver location to the point of integration (inside the ball), $n = \frac{\mathbf{x}' - \mathbf{x_R}}{|\mathbf{x}' - \mathbf{x_R}|}$ as derived in [3]. The magnetization **M**, *inside the ball, is given by (FID Signal)*

$$M_x(t) = M^{eq} e^{-t/T_2} cos(\omega_0 t) \tag{2.37}$$

$$M_y(t) = -M^{eq} e^{-t/T_2} sin(\omega_0 t) \tag{2.38}$$

$$M_z(t) = M^{eq}(1 - e^{-t/T_1}) \tag{2.39}$$

where $\omega_0 = \gamma B_0$ is the Larmor frequency, T_2 and T_1 are the transverse and longitudinal relaxation times and M_eq is the magnetization at equilibrium. With this derivation from [3], it is clear that both permittivity and conductivity are presented in both equations and, thus, theoretically affect the resulting signal.

Observe that in both equations 2.35 and 2.36, the signal components are inversely proportional to either $|\mathbf{x}' - \mathbf{x_R}|^2$ or $|\mathbf{x}' - \mathbf{x_R}|^3$ and thus the received signal's SNR is expected to decrease as the distance increases. Furthermore, the magnitude of the Magnetization M_{eq} plays a significant role, as the higher it is, the higher the SNR of the received signal. Investigating whether the antenna's orientation affects the resulting measured signal is also interesting. Based on the formulation of the FID signal, equations 2.37,2.38,2.39 the orientation to be tested in for z- direction and x, y-direction.

To achieve the retrieval of dielectric properties in [3], they formulated and solved a least squares problem. Figure 2.4 shows the relative error for retrieving the dielectric properties by placing the receiver across the z-axis and varying its distance from 0 to 2 meters from the ball.

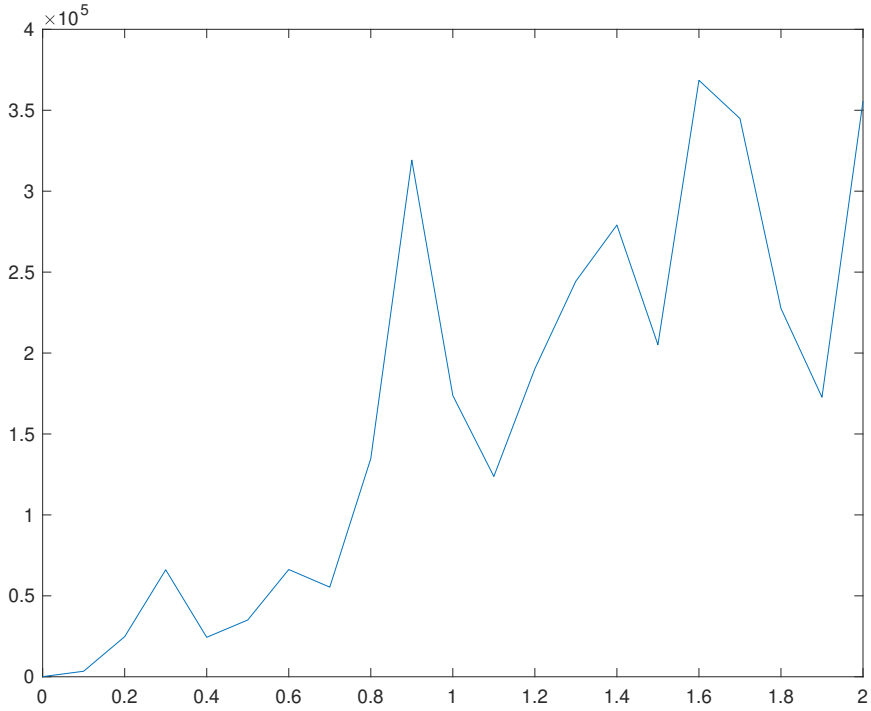

Figure 2.4: Relative error between retrieved and real dielectric properties, evaluated by varying the receiver location in simulation along the z-axis

This is because the main magnetization component contributing to the signal is the z-component which has a much lower amplitude than x and y; thus, the induced voltage has a low SNR. The simulated voltage can be seen in Figure 2.5 for $\overrightarrow{\nu} = \overrightarrow{z}$ *and in Figure 2.6 for* $\overrightarrow{\nu} = \overrightarrow{x}$

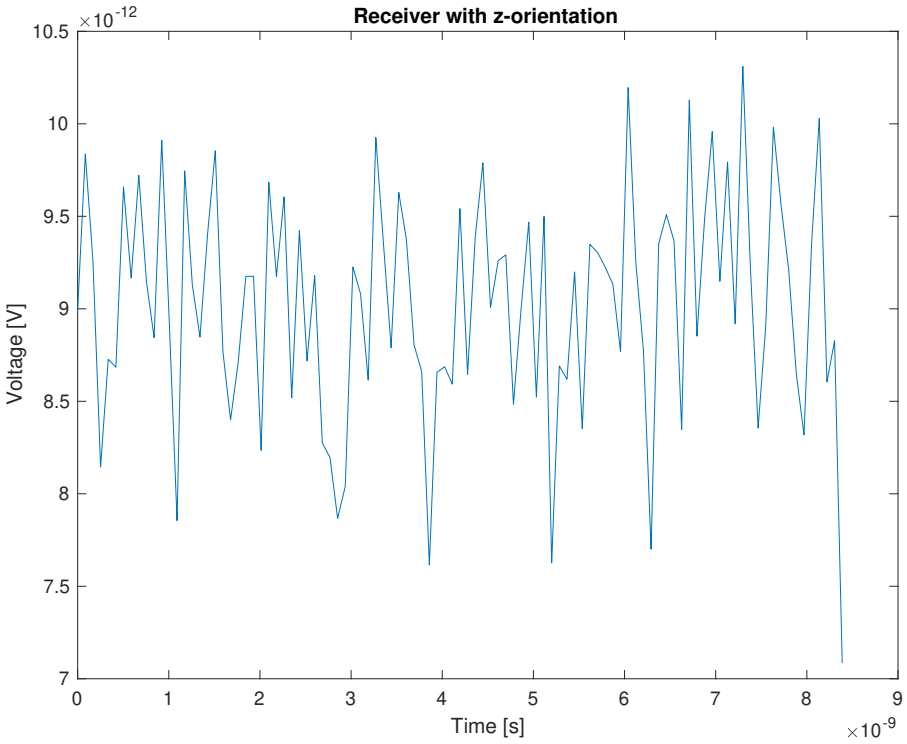

Figure 2.5: Induced voltage across receiver's coil when receiver orientation vector $\overrightarrow{\nu} = \overrightarrow{z}$

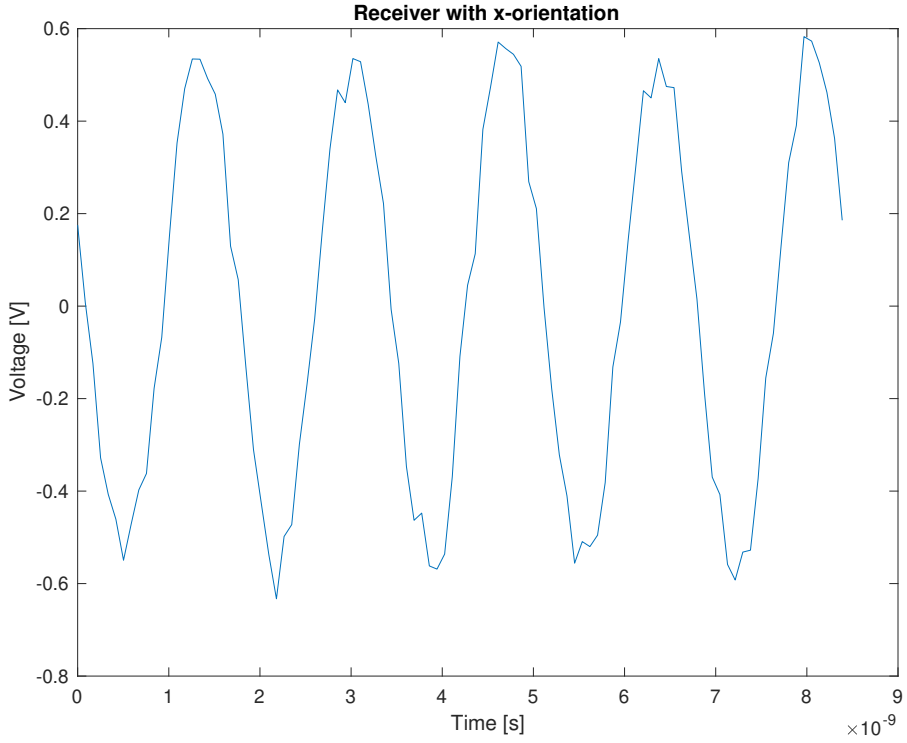

Figure 2.6: Induced voltage across receiver's coil when receiver orientation vector $\overrightarrow{\nu} = \overrightarrow{x}$

Up to this point, it is clear that under many assumptions introduced in [3], and by meeting several conditions, dielectric properties using the generalized signal model can be retrieved in theory. Moreover, using the generalized signal model, the dielectric properties were never retrieved from an object in vitro. Therefore, the primary goal of this research is to evaluate whether and how dielectric properties affect the received signal and whether a relation between the dielectric properties and the received signal can be derived to later retrieve dielectric properties in vitro using this model. Therefore, one of the research questions to be investigated is how sensitive the generalized model is to several factors, such as magnetic field strength, the distance of the receiver coil, orientation, and the excitation sequence.

3

The effect of Dielectric on a single emitting loop's magnetic field

In this chapter, the simulations conducted before the experiment are presented. The goal is to cover the following:

- *Initially, the aim is to verify whether the analytical expression for a small emitting loop (magnetic dipole) aligns with the simulated emitting loop. This verification is highly important as the single emitting loop is the fundamental element for designing excitation sequences later in this chapter. The emitting loop is evaluated by comparing the electromagnetic fields at identical locations and orientations to the ball's position.*
- *Following the emitting loop validation, the effects on the resulting magnetic fields of placing the emitting loop inside a dielectric solution and varying the conductivity and permittivity of the solution inside the ball are explored.*
- *Furthermore, to simulate the excitation sequence used during the experiment, the effect on the magnetic field by a series of loops is assessed similarly, and the resulting fields are investigated.*
- *Lastly, to simulate the experimental setup, a spherical plastic layer is added to the exterior of the dielectric solution, simulating the plastic ball used in the experiment, containing the water-based dielectric solution*

For the rest of this report, the standard axis convention will be used as shown in Figure 3.1

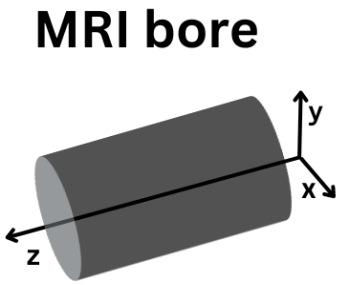

Figure 3.1: MRI axis convention

3.1. Analytical and Simulated magnetic field of a single emitting loop

The primary objective of this section is to conduct a computational simulation of a single emitting loop and compare its behavior with the analytical models and simulations presented in [3]. More specifically, this part of the research aims to do the following:

- *Validate the Electromagnetic Field equations. The first task is to validate that both analytical expressions and computational simulations would yield comparable electromagnetic fields when the loops are not submerged into a dielectric solution. This is essential since the real-world application of these loops involves certain variations in parameters such as geometric dimensions, and material properties, that may cause large deviations between simulation results and analytical results.*
- *Mutual Inductance Analysis. Following the validation process, the mutual inductance between the simulated loop and the receiver coil was quantified. This metric, mutual inductance, serves as a metric of comparison for analyzing whether the loop under study aligns with potential receiver setups that were used later in the experiment.*
- *Influence of dielectric material. After validating the electromagnetic field characteristics of the loop, an initial simulation was performed to check whether submerging the loop into a dielectric solution would indeed show alterations in the electromagnetic field. More specifically, the magnetic field components (H_x, H_y, H_z) were compared between the two scenarios at a distance away from the loop.*

The analytical expression, derived in [14], of the magnetic field for a current-carrying thin loop wire at a point **x** *can be divided into three components: near field, intermediate field, and far field. The total field of the j-th component is given by*

$$H_j = H_j^{NF} + H_j^{IF} + H_j^{FF}, for j = x, y, z \tag{3.1}$$

where

$$H_j^{NF} = (3 \sum_{n=x,y,z} \Xi_j \Xi_n - m_j(s)) \frac{exp(-\gamma|X|)}{4\pi|X|^3} \tag{3.2}$$

$$H_j^{IF} = \gamma(3 \sum_{n=x,y,z} \Xi_j \Xi_n - m_j(s)) \frac{exp(-\gamma|X|)}{4\pi|X|^2} \tag{3.3}$$

$$H_j^{FF} = \gamma^2(\sum_{n=x,y,z} \Xi_j \Xi_n - m_j(s)) \frac{exp(-\gamma|X|)}{4\pi|X|} \tag{3.4}$$

where

$$\mathbf{X} = \mathbf{x} - \mathbf{b} \tag{3.5}$$

With **x** *being the point of observation and* **b** *being the barycenter of the loop and,*

$$\Xi_j = \mathbf{X_j}/|\mathbf{X}|, \tag{3.6}$$

being the j-th component of the unit vector pointing from the center of the loop to the point of observation and

$$m_j(s) = I(s) \int_{x \in S} dA_j \tag{3.7}$$

is the magnetic moment of the loop. Note that the above equations 3.2, 3.3, 3.4 make use of the Einstein notation [14].

To simulate a single emitting loop, Sim4Life (S4L),a software developed by Zurich MedTech AG, was used. It primarily simulates and analyzes electromagnetic fields interacting with biological tissues using human phantoms in electromagnetic fields.

3.1.1. Discretization of Maxwell's Equations

S4L is using the Finite-Difference Time-Domain method (FDTD). The FDTD method was originally introduced by Yee. It is a direct solution, in the time domain, of Maxwell's curl equations. The spatial allocation of electric field (E-field) and magnetic field (H-field) components occurs on a staggered mesh within a Cartesian coordinate system and can be seen in Figure 3.2.

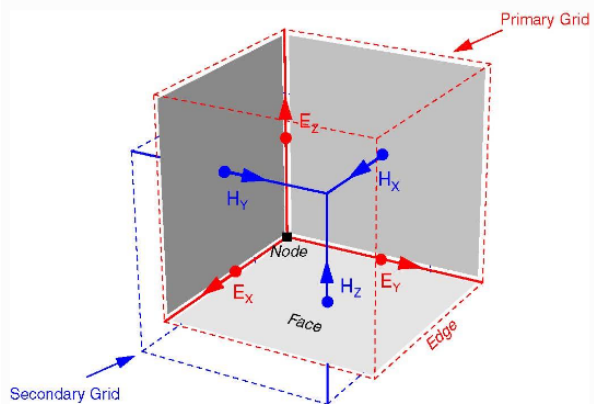

Figure 3.2: E and H x,y,z components in a 3D Yee cell, shown on a staggered grid, image source: S4L documentation

3.1.2. Analytical vs S4L - Results

The loop configured in S4L, is depicted in Figure 3.3. The loop follows an octagonal geometric shape, with each of its sides having a 4mm length. The internal angles between each of the sides are 45 *degrees. Lastly, the thickness of each of the sides of the loop is 0.1 mm. The settings are summarized in Table 3.1.*

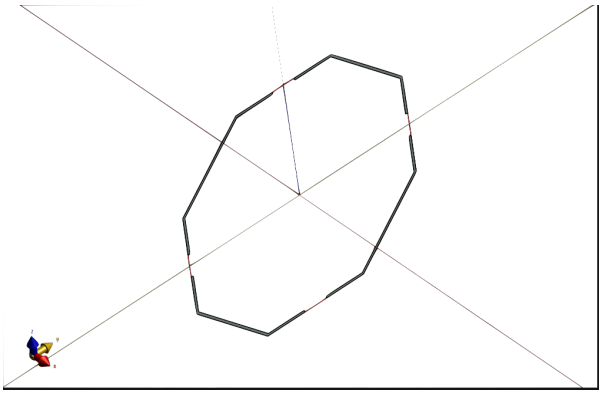

Figure 3.3: Thin Loop in S4L

Settings	Value	Unit of measure
Shape	Octagonal	-
Side length	4	mm
Side angle	45	degrees (°)
Thickness	0.1	mm

Table 3.1: Single loop settings used in S4L simulation

Before initiating the simulation in S4L, it is crucial to calibrate the resonance frequency of the emitting loop. The resonant frequency was set to 298 MHz to match the operating frequency of a 7T MRI. The loop's resonance frequency is at the absolute impedance peak frequency. So, a broadband simulation is performed to get the impedance against the frequencies graph as depicted in Figure 3.4.

The capacitors' value can be calculated using

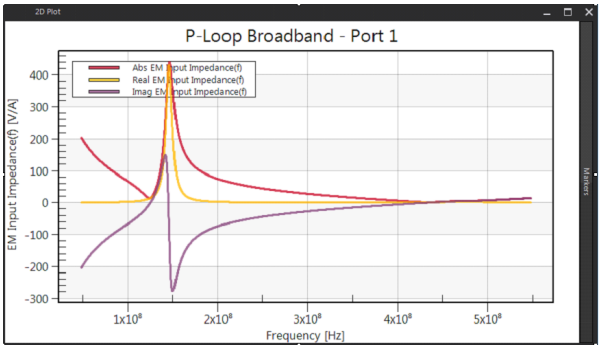

Figure 3.4: Impedance graph of a single loop for a broadband simulation

$$2\pi f_{resonance} = \frac{1}{\sqrt{LC_{total}}} \tag{3.8}$$

By solving for C_{total} the capacitors' value was calculated at 10 pF, and they have been tuned such that the coil resonates at 298 MHz, as depicted in Figure 3.5.

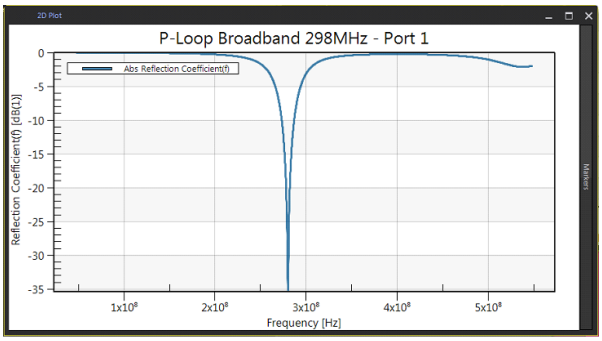

Figure 3.5: Impedance graph of a single loop for a broadband simulation

After simulating the single emitting loop, Matlab was utilized to process the obtained results. Using S4L, we were able to extract the grid, B-field, H-field, and E-field components for every point on the grid in relation to their respective x, y, and z coordinates. Thus, the calculation of the H-field using the analytical expression was performed on the same coordinates using the grid location extracted from S4L. Figure 3.6 shows that at the location $z = 0$, the z component H_z of the resulting field is zero throughout the XY plane, as expected. Magnetic field lines are parallel to the XY-Plane at $z = 0$; thus, the z component is zero in the entire plane.

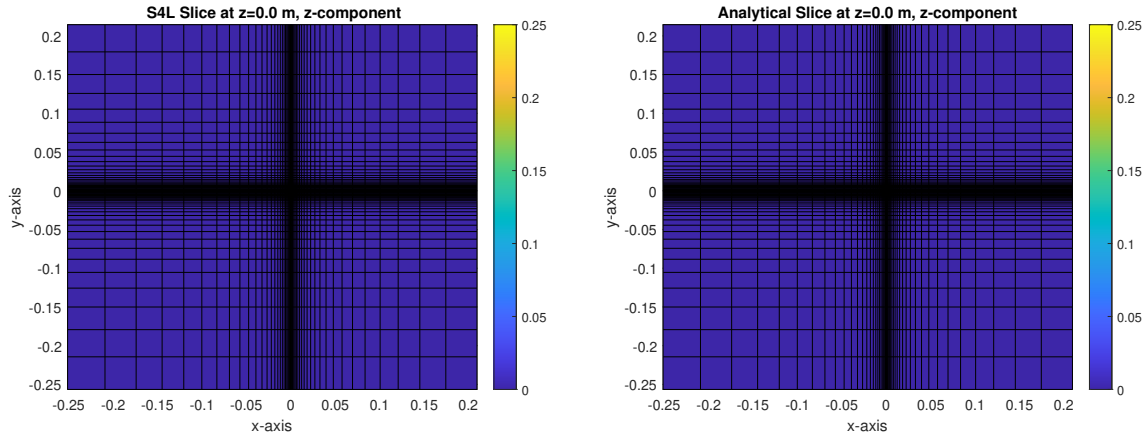

((a)) Z component of the magnetic field, S4L simulation

((b)) Z component of the magnetic field, analytical expression

Figure 3.6: On the right (b), the magnetic field as calculated by the analytical expression, and on the left (a), the magnetic field in Sim4Life

In Figures 3.7,3.8,3.9, the magnetic field's x,y, and z-components are shown respectively. The simulated field is shown on the left, and the field calculated by the analytical expression on the right. Observe that the field's voxels are non-uniform; thus, the closer we get to the center where the loop is located, the smaller the voxels' size. That is the reason black lines appear at the center of the graphs. The same grid has been used when calculating the field using the analytical expression to compare both fields. Voxelization is performed automatically by S4L.

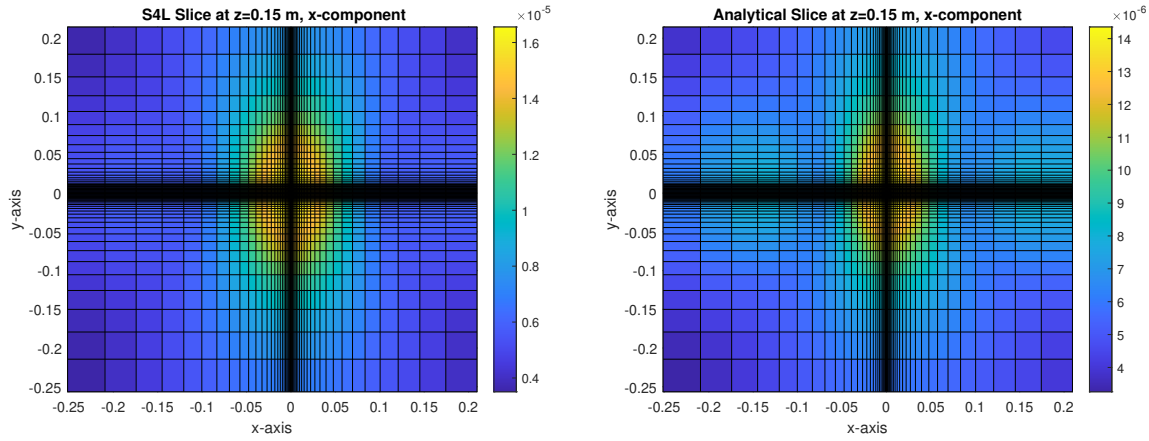

((a)) x component of the magnetic field, S4L simulation

((b)) x component of the magnetic field, analytical expression

Figure 3.7: On the right (b), the magnetic field as calculated by the analytical expression, and on the left (a), the magnetic field in Sim4Life

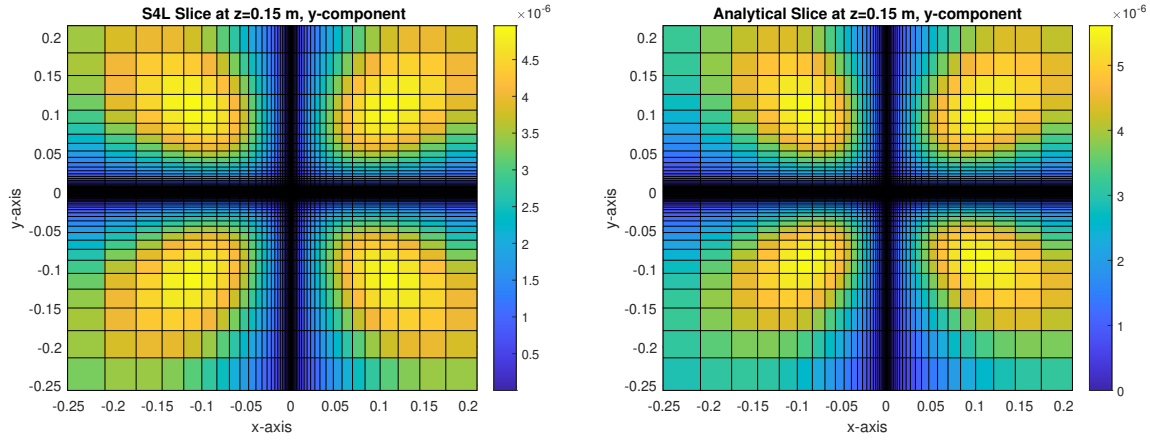

((a)) y component of the magnetic field, S4L simulation

((b)) y component of the magnetic field, analytical expression

Figure 3.8: On the right (b), the magnetic field as calculated by the analytical expression, and on the left (a), the magnetic field in Sim4Life

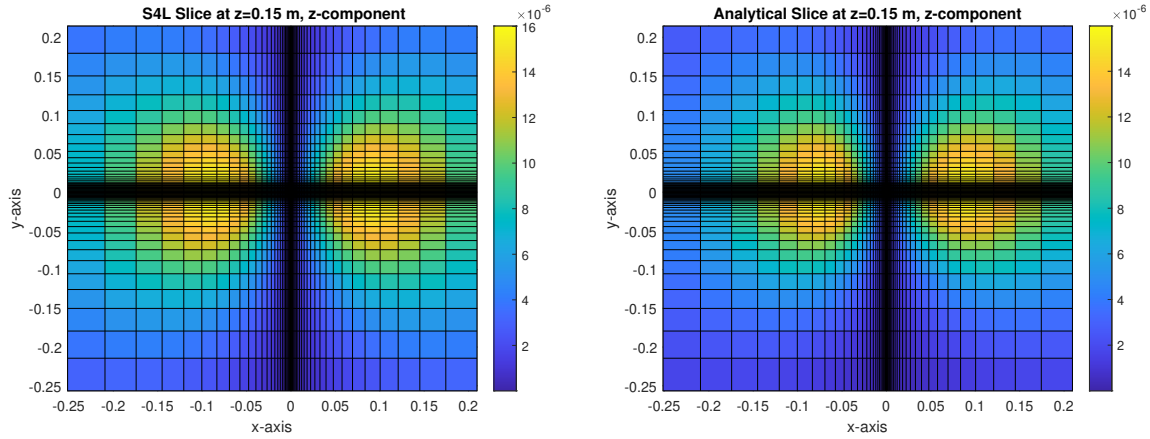

((a)) z component of the magnetic field, S4L simulation

((b)) z component of the magnetic field, analytical expression

Figure 3.9: On the right (b), the magnetic field as calculated by the analytical expression, and on the left (a), the magnetic field in Sim4Life

3.1.3. Simulation results - magnetic field strength

The small differences in the magnetic field strength between the analytical model and the simulation in S4L can be explained by various factors. The first factor is the thin-wire assumption of the analytical model. In the calculations of this model the diameter of the wire is not taken into account in the calculations. This is, of course, a simplification and an assumption made to create a simpler equation for this non-real-life model. However, this assumption disregards a wire's electric properties compared to the S4L simulation. Furthermore, the loop has a perfect circular geometry in the analytical model, whereas, in S4L, it has an octagonal shape. These geometrical differences result in nuances in the distribution of the electromagnetic field. Last but not least, unlike the analytical model, which does not take into account any material properties, S4L uses FDTD solvers, which require a material to be assigned for all objects in the simulation. In these simulations of the coil, a perfect electric conductor was assigned. The surrounding medium was modeled as air, and the direction of B_0 is towards positive z-direction as depicted in Figure 3.1. When performing comparative studies between analytical and S4L simulations, one has to take into account these differences in both models and be careful when performing a straightforward comparison of field strength. By observing the fields of both analytical and simulated spatial components, one can safely say that magnetic field lines follow the same pattern, with minor differences in strength values due to all the aforementioned reasons.

3.1.4. Receiver's location - mutual Inductance

In the previous section, we investigated whether a single emitting loop can simulate a magnetic dipole. Before the experiment, an important question had to be answered. What would be the optimal positioning of the receiver coil in relation to the emitting coil? On the one hand, by placing the receiver too far from the emitting coil, we are at risk of having low sensitivity due to the attenuation of the magnetic field strength in the far field. Thus, differences due to varying conductivity of the dielectric solution might not be able to be observed. On the other hand, it is expected that the differences in magnetic field lines are larger if we get very close to the receiver.

To answer these questions, the following are performed:

- *The differences in the amplitude of the resulting H_x, H_y and H_z components is compared*
- *The mutual inductance between the emitting coil and the receiving coil was calculated at various distances in the near, medium, and far fields.*

Figures 3.7(b), 3.8(b), 3.9(b), show the H-field calculated on these grid location extracted from S4L. To measure the similarity of the B-fields at the receiver location Faraday's Law was used. By summing the B-field strength (in frequency domain) inside the area covered by the notional receiver, according to Faradays law

$$\oint E.dl = -j\omega \int \int BdA \tag{3.9}$$

In the configuration under examination, the orientation of the receiver coil is carefully chosen to be facing the z-axis. This is in contrast to the orientation of the emitting loop, which is fixed along the x-axis, with its magnetic moment specifically directed towards the positive x-direction. The setup is depicted in Figure 3.10, with the green circle being the emitting loop and the blue lines the receiver in different locations along the z-axis.

Figure 3.10: Orientations of emitting and receiver loops

These configurations and their associated mutual inductance components are visually represented in Figures 3.11, 3.12, and 3.13.

By observing from these Figures,3.11, 3.12, and 3.13, we see the varying degree of mutual inductance based on the relative position of the receiver coil to the emitting coil's origin. It's critical to note that the deviations between the computed mutual inductance values are larger when the receiver is located close to the single emitting loop. This is due to the more complex electromagnetic phenomena taking place in the near-field region compared to the far-field region. Specifically, the near-field region is characterized by non-propagating fields that contribute to the difference between the analytical and simulated models.

As mentioned, these differences may be the result of several factors. The analytical models often simplify the physical constraints to develop manageable mathematical expressions, while numerical FDTD simulations utilize more real-world properties. These nuances become very noticeable in the near-field where the mutual inductance between the two coils is more sensitive to these parameters.

Therefore, when interpreting these results, it is crucial not only to consider the coils' orientation/ magnetic moment direction but also the near-field or far-field—in which these interactions are occurring. These factors clearly influence the mutual inductance values and should be taken into account when deciding the receiver location.

To quantify the similarity between the analytical and simulated of the emitting single loop, the correlation coefficient along the z-axis of a point $(x = 55mm, y = 55mm)$ inside the area of the receiver is calculated, for the H-field and E-field. The results are shown in Figures 3.14 and 3.15, respectively.

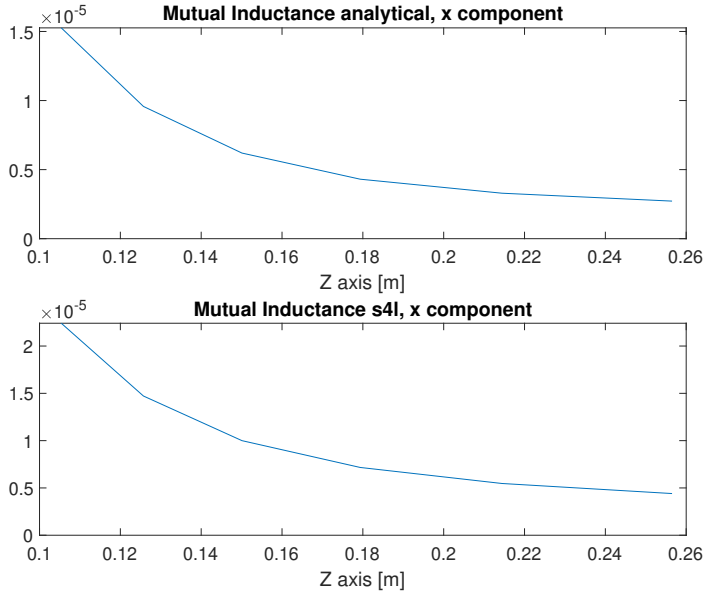

Figure 3.11: X-component of Mutual inductance against receiver's location

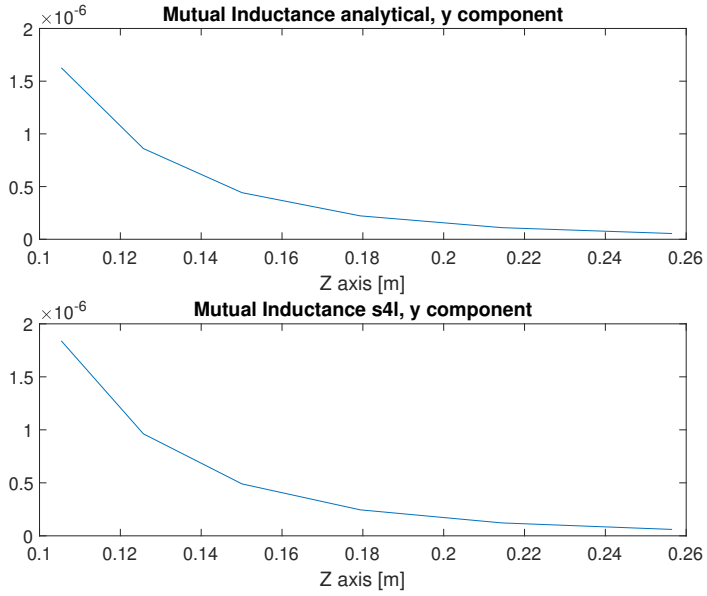

Figure 3.12: Y-component of Mutual inductance against receiver's location

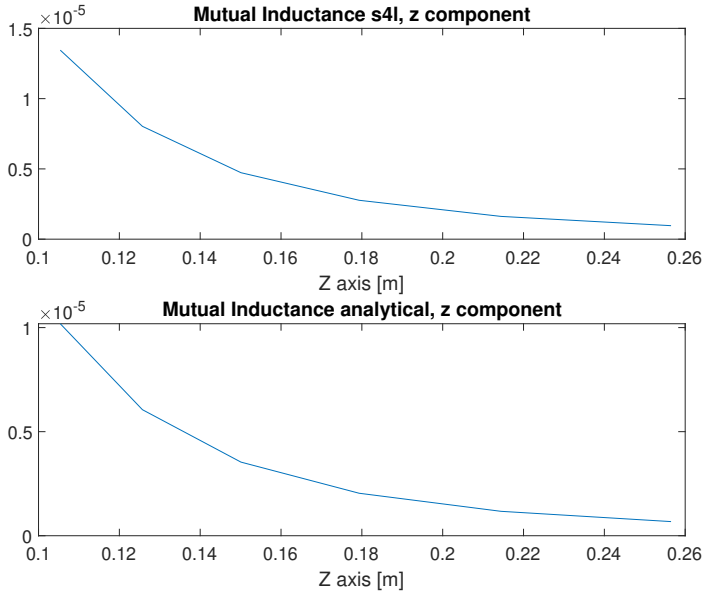

Figure 3.13: Z-component of Mutual inductance against receiver's location

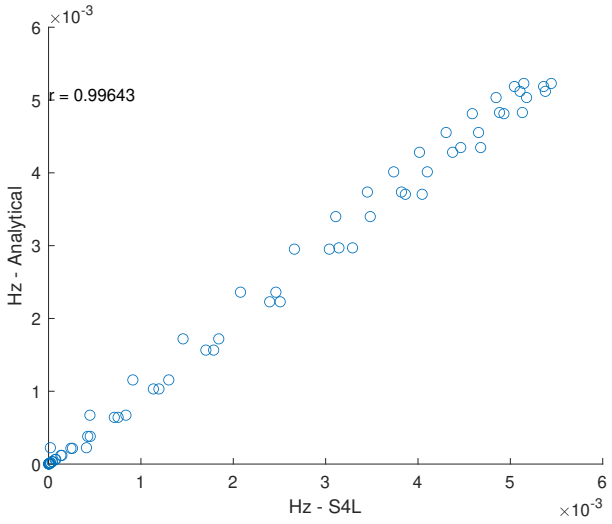

Figure 3.14: Correlation across z axis, between analytical and simulated Hz-component at the point x = 55mm,y=55mm, point within the receiver loop

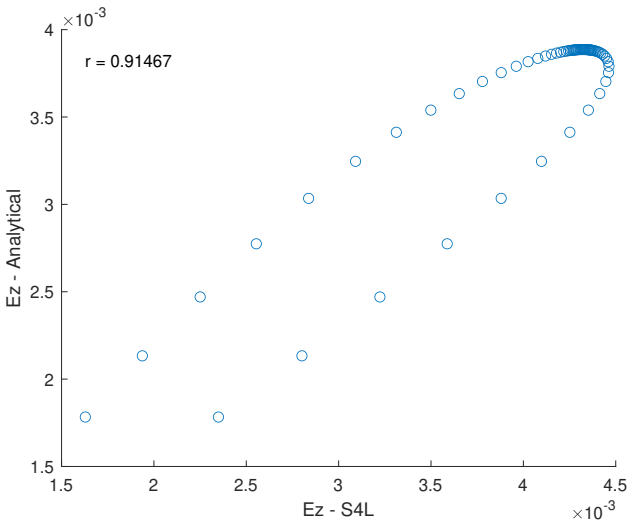

Figure 3.15: Correlation across z axis, between analytical and simulated Ez-component at the point x = 55mm,y=55mm, point within the receiver loop

As can be seen, the correlation of the mutual inductance for H_z is 0.99643, and for E_z, it is 0.91467.

3.2. The effect on the H-field produced by a small emitting loop inside a dielectric

3.2.1. Dielectric solution with relative permittivity $\epsilon_r = 1$

In the previous sections, it is seen that the simulated and analytical expressions of a loop are similar. With this foundational understanding, we are now able to extend our research into more specialized conditions. In short, investigate the effect of varying conductivity. Observe that in equation 2.35, we have three main contributing terms. The last two are dependent on σ and ϵ_r, respectively. The first term is a constant. By setting $\epsilon_r = 1$, we eliminated the last term. By replacing the second partial derivative with $-\omega^2$, the equation now has an initial amplitude, and then by increasing σ, the amplitude gets smaller, which is exactly the behavior expected to be observed. Note that the equation 2.35 requires the whole ball to be magnetized, whereas in our case, there's only an emitting loop inside the ball. So, If the terms inside the integral are not zero, this is the intended behavior. Figure 3.16 shows a visual representation of the simulation setup.

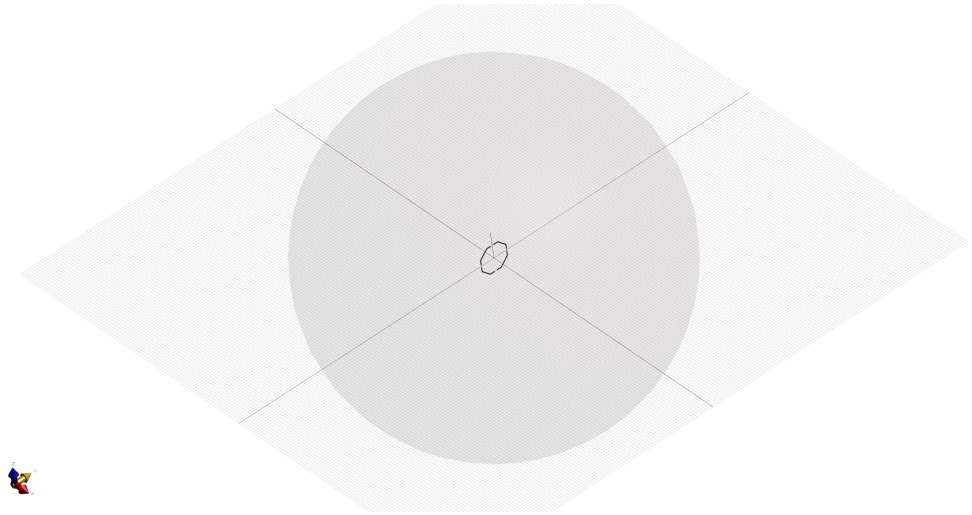

Figure 3.16: Simulation setup, to investigate the effect of dielectric on the field produced by single emitting loop

The receiver coil was placed right next to the ball facing the positive z-axis, and the emitting loop had a magnetic moment on the positive x-axis. The setup is depicted in Figure 3.17; the receiver was located at coordinates $x = 11.5cm, y = 0cm, z = 0cm$. *The diameter of the receiver coil is* $11cm$, *and the dielectric sphere is* $12cm$.

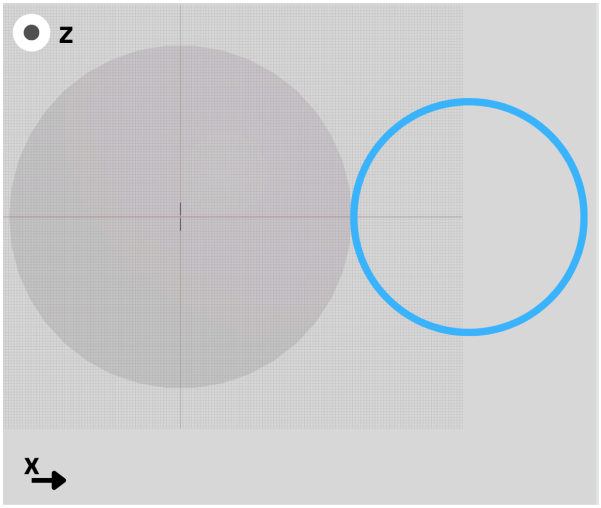

Figure 3.17: Simulation setup, receiver loop is shown as the blue circle.

Note that a dual-source arrangement was used to generate a symmetrical magnetic field. In this arrangement, the two sources are placed diametrically opposite to each other. A phase shift of 180 degrees was introduced to one of these sources. This phase-shifted source decision is introduced to counterbalance asymmetries that arose due to a resulting non-uniform magnetic field at the receiver location, thereby ensuring a magnetic field that exhibits spatial uniformity and symmetry to the extent that is possible.

For details of the configuration settings used in this simulation, refer to Table 3.2 as it shows the properties of the source.

Source settings	**Value**	**Unit of measure**
Excitation signal	Harmonic	-
Frequency	298	MHz
Type	Voltage	-
Amplitude	1	V
Delayed periods	0	-
Resistance	50	Ohm
Distribute along line	True	-

Table 3.2: Source settings for single loop used in S4L

The properties of the dielectric solution can be seen in Table 3.3.

Property in S4L simulation	**Value**	**Unit of measure**
Type	Dielectric	-
Mass density	1000	kg/mˆ3
Electric conductivity range	0.0 - 0.8	S/m
Relative permittivity	1	-
Relative permeability	1	-
Magnetic conductivity	0	Ohm/m

Table 3.3: Dielectric medium settings, for single loop simulation in S4L

Table 3.4 shows the parameters of the emitting loop used in the simulations.

Stripline width	1 mm
Loop width	10 mm
Loop Height	10 mm
Loop thickness	0.2 mm
Corner angle	45 degrees
Corner length	4mm

Table 3.4: Properties of the loop used in S4L

After running the simulation, the B field and grid were extracted and processed using Matlab (see code in Appendix). By applying Faraday's law of induction, one can derive the Electromotive force. This is expressed as

$$V = -j\omega \int B.dA \tag{3.10}$$

The B-field traversed through the receiving coil is summed up. Because the grid is non-uniform, each contribution of the magnetic flux passing through the receiving coil is multiplied by the area of the cell A. This area-weighing is crucial, as it ensures that cells with different sizing do not equally contribute to the calculation of the induced voltage. This calculation was performed for all simulated conductivity values. The results are presented in Figure 3.18.

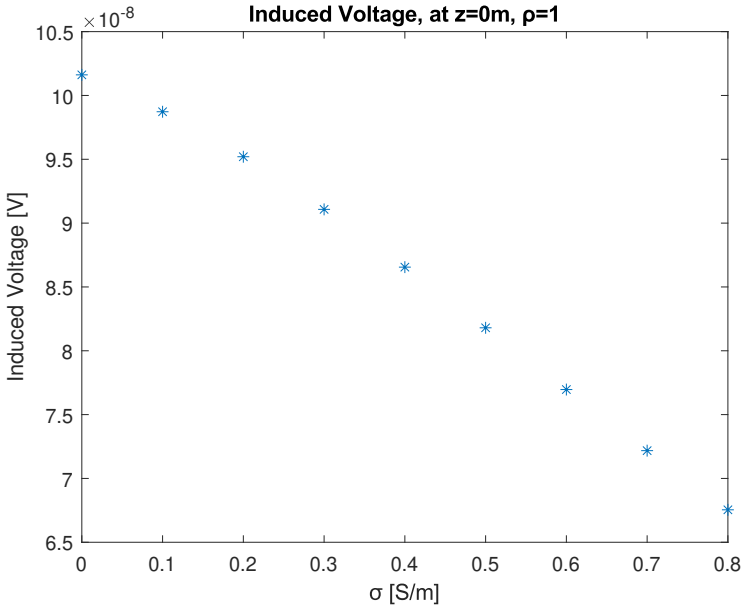

Figure 3.18: Induced voltage at receiver location z=0m

The expected behavior is observed, as conductivity increases the amplitude decreases.

3.2.2. Dielectric solution with relative permittivity $\epsilon_r = 80$

Using a similar approach as before, we changed the relative permittivity to 80 so we can simulate the change of behavior when ϵ_r is not equal to 1. The reason for choosing $\epsilon_r = 80$ is that this is the relative permittivity of water. The simulation was performed with the parameters in Table 3.5,

Figure 3.19 shows the results for the same simulation as in 3.18 but for $\epsilon_r = 80$.

Stripline width	1 mm
Loop width	10 mm
Loop Height	10 mm
Loop thickness	0.2 mm
Corner angle	45 degrees
Corner length	4mm
Conductivity range	0.0 - 0.8 S/m
Relative Permitivity	80

Table 3.5: Loop properties used in S4L for relative permittivity=80

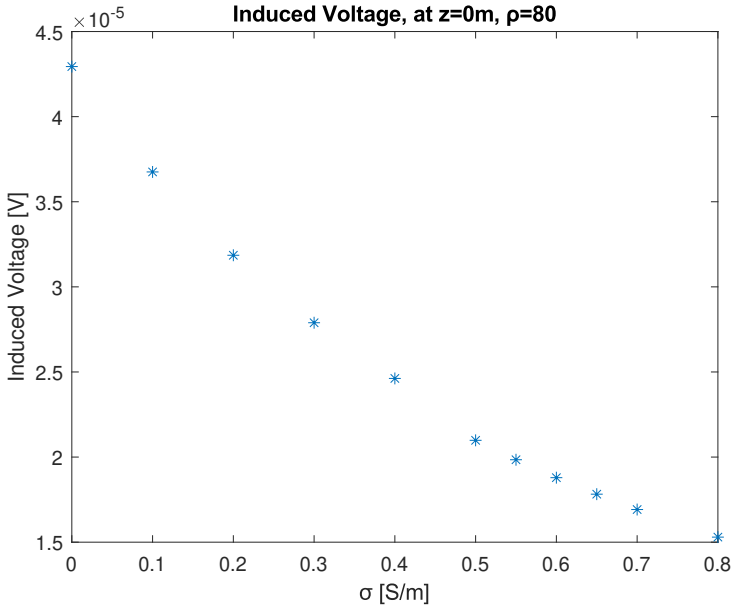

Figure 3.19: Induced voltage at receiver location z=0m

As it can be observed, Figure 3.19 follows almost the same trend as before. However, a non-linear relation is now observed. The main difference is that the value at $\sigma = 0$ is larger. This can be explained by the fact that now the last term of 2.35 is not zero anymore.

3.3. The effect on the H-field produced by emitting loops in series forming a cylinder inside a dielectric

To bring S4L simulations closer to the real MRI experiment, beam excitation needed to be introduced. To accomplish this an arrangement consisting of single loops in series was introduced. This arrangement provides a more uniform excitation and mimics better the MRI excitation. The S4L configuration can be inspected in Figure 3.20.

It is essential to highlight that beam excitation differs fundamentally from the one described in [3]. However, our primary objective is not to fully replicate the exact setup from the literature. By using this excitation setup, we're effectively extending the scope of this research. We're not only assessing the impact of conductivity on magnetic field strength but also testing how a beam excitation will alter the outcome.

The results of the simulation can be seen in Figure 3.21.

Compared to the previous setup, which used a single emitting loop, here the graph follows a non-linear behavior. The induced voltage seems to follow a parabolic behavior as σ increases.

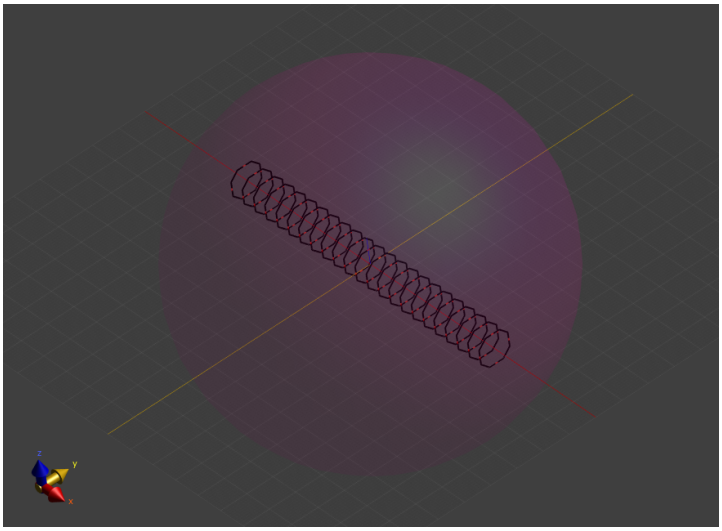

Figure 3.20: Simulation setup, to investigate the effect of dielectric on the field produced by a series of loops, simulating MRI beam excitation

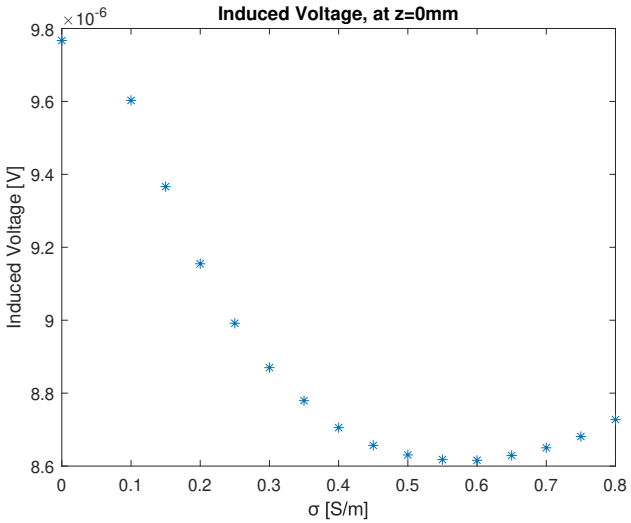

Figure 3.21: Induced voltage, from a field produced by a series of loops, by varying conductivity for $\epsilon_r = 1$

3.4. The effect on the H-field produced by emitting loops in series forming a cylinder inside a dielectric, covered by plastic

In the simulation, a small plastic ball is used to enclose the dielectric solution. Thus, an extra layer of plastic has to cover the dielectric. This has been simulated, and the setup can be seen in Figure 3.22. The outer layer consists of a 1mm plastic with $\epsilon_r = 2.4$ *and* $\sigma = 0$.

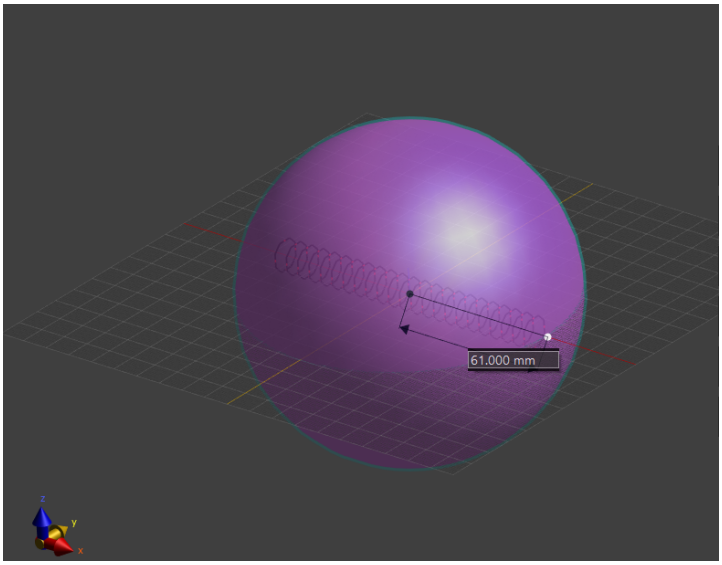

Figure 3.22: Simulation setup, to investigate the effect of dielectric inside a small ball on the field produced by a series of loops, simulating MRI beam excitation

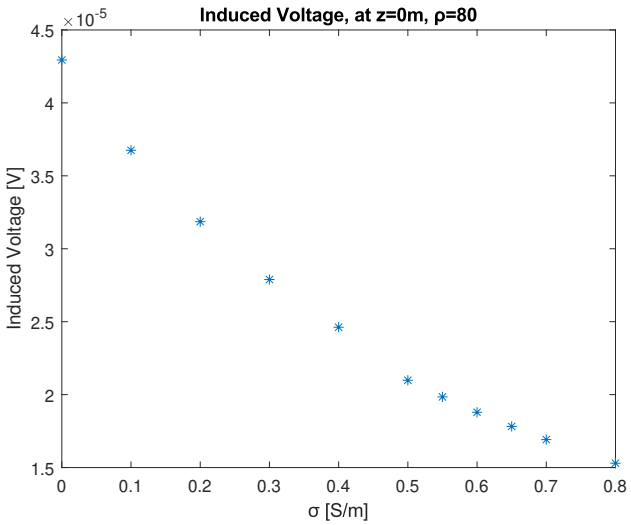

Figure 3.23: Induced voltage at receiver location z=0cm

3.5. Summary of key findings

As presented in this chapter, the simulations have yielded clear results, building a strong case for our main hypothesis. It is observed that the conductivity of a dielectric solution, when varied, influences the resulting magnetic field strength after excitation. These changes in the solution's charge density affect the solution's ability to interact with and change the scattered electromagnetic field, thus leading to differences in the resulting magnetic field strength. More specifically, at $z = 0m$, the highest mutual inductance between the emitting loop and the receiver coil is observed. Thus, placing the receiver coil at $z = 0$ will be beneficial to measure the effect of increasing σ due to scattered fields. Moreover, it is expected that when $\sigma = 0$ and $\epsilon_r = 80$, we will observe a stronger signal at the receiver. When we apply a beam excitation, it is anticipated to get a non-linear relationship between increasing conductivity and the measured signal strength.

4

Experiment

4.1. Introduction

This chapter aims to validate the findings of the simulations through an experiment and whether what is observed in simulations can be measured through the experiment. The correlation between increasing conductivity and getting a lower magnetic field strength provides a strong case for this research's main hypothesis: that there exists a clear, direct, distinguishable, and measurable relationship between the conductivity of a dielectric solution and the strength of the induced magnetic field after exciting the dielectric solution.

4.2. Experiment setup and scan properties

Using the facilities of the University Medical Center Utrecht, a 3T MRI system was used for the experiment, as shown in Figure 4.1, facilitated by the Department of Radiology.

The experimental setup is depicted in Figure 4.2. Note that in the setup image, two coils are shown. However, the coil with the red X has not been used. A plastic sphere with a 120mm diameter is placed in the center. The thickness of the plastic is 1mm. The sphere was filled with distilled water to achieve the lowest possible conductivity, as distilled water is deionized. To study the impact of increasing conductivity, we enhanced the solution conductivity by sequentially adding 1 gr of sodium chloride by extracting some water from the sphere, dissolving salt in it, and injecting it back into the sphere.

The first obstacle that we faced was during the initial survey scan. In short, a survey scan is a low-resolution scan that is quickly taken with the purpose of orienting the object properly. The images resulting from the survey scan had a very low contrast. This phenomenon was due to the fact that the sphere in the MRI couldn't be "sensed" by the MRI's receiver coils. To overcome this problem, gadolinium was added to the dielectric solution. Gadolinium is an earth metal, and it is used as an MRI contrast agent to enhance the resulting scan image contrast by reducing the T1 relaxation time of water protons.

The experiment was executed by using a T1-weighted Fast Field Echo (T1FFE) sequence. This sequence was chosen for its ability to differentiate tissues based on their T1 relaxation times. The specific parameters used in the scanning are given in the Table 4.1.

4.3. Experiment results

The data acquired directly from the MRI scanner is not in a form that one can immediately conduct a direct comparison or analysis. Therefore, the raw data needed to be transformed. The output file of the MRI scan is in the form of magnitude images. These plots are exported as .REC files are matrices of pixel values representing the measured signal intensity at each voxel. Although the pixel data can be useful for medical doctors, using it directly to perform comparisons between the various scans can be misleading due to variations in the resulting magnitude image, equipment calibrations, etc.

Next to the .REC file, there's an associated .PAR file that holds data about the scan. This data includes details that can help in rescaling the raw pixel values to a standard form, thus making it possible

Figure 4.1: Image of the MRI machine used for the experiment

to compare individual scans. More specifically, three parameters helped to achieve this: the rescale slope (RS), the rescale intercept (RI), and the scaling slope (SS) by using the following formula,

$$RV = \frac{PV * RS + RI}{RS * SS} \tag{4.1}$$

The rescaled magnitude plot, for $\sigma = 0$, can be seen in Figure 4.3. Observe that the sphere does not have the same magnitude everywhere. This is because the receiving coil is placed right next to the ball, and the closer the ball is to the receiving coil, the higher the signal. In order to compare all the measurements for all the conductivity values, a mask was introduced in the middle of the sphere. This allows us to compensate for small errors occurring when placing the sphere back in its place after the salt addition between scans.

By calculating the masks, two metrics were chosen. The first one is the max magnitude value of the mask and the standard deviation. Both can be observed in Figures 4.4 and 4.5 respectively. The maximum value does show some minor trends. By increasing the conductivity, the max value is also increasing. However, the standard deviation increases too. Thus, a solid relation can not be derived from this experiment. This can be because differences due to dielectric properties are too small and can not be sensed by the receiver coil. However, we can see a big difference between $\sigma = 0$ and $\sigma = 0.2$, which is the only indication that increasing conductivity affects the resulting magnetic field strength. Although this can be seen in the figures, the simulation trends can not be verified yet. In order to achieve that, a higher-frequency MRI can be used as it might help to sense those differences.

Figure 4.2: Image of the experimental setup

Scan Duration	12.6 seconds
Patient Position	Head First Supine
Preparation Direction	Right-Left
Scan Resolution	80 x 80
Repetition Time (TR)	150 milliseconds
Field of View (FOV)	240.000mm (ap), 5.000mm (fh), 240.000mm (rl)
Water Fat Shift	0.870 pixels
Off Centre midslice	31.062mm (ap), -3.006mm (fh), 11.022mm (rl)

Table 4.1: Experiment MRI parameters

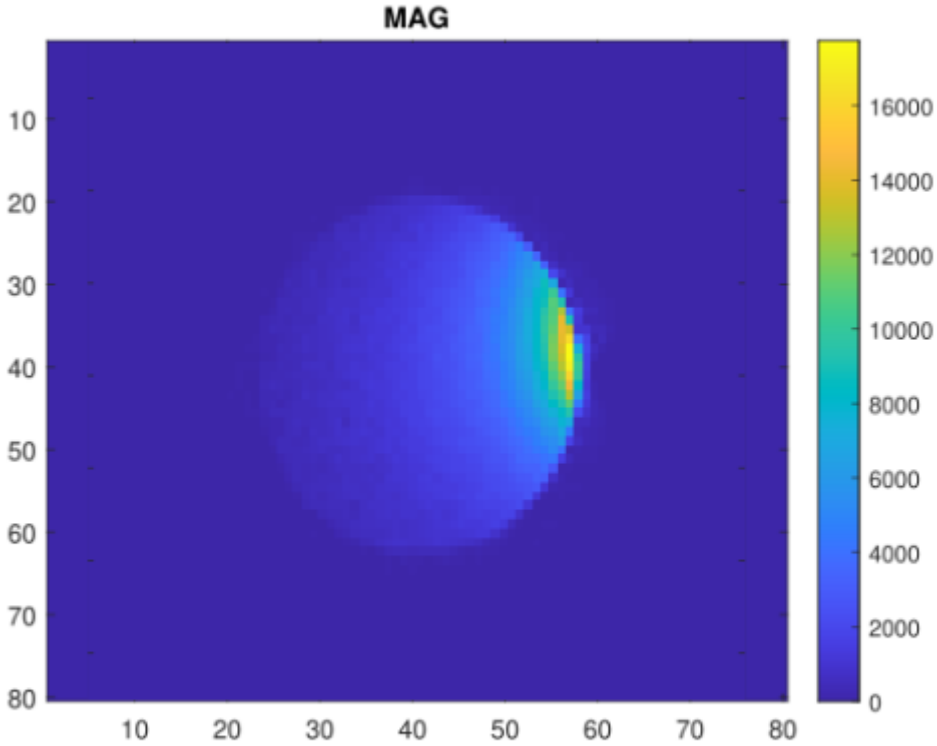

Figure 4.3: Experiment resulting magnitude plot

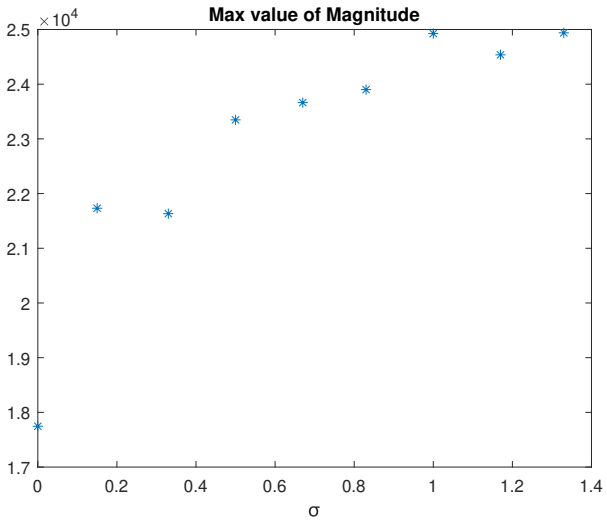

Figure 4.4: Maximum value of the masked magnitude plot for all the experiment scans

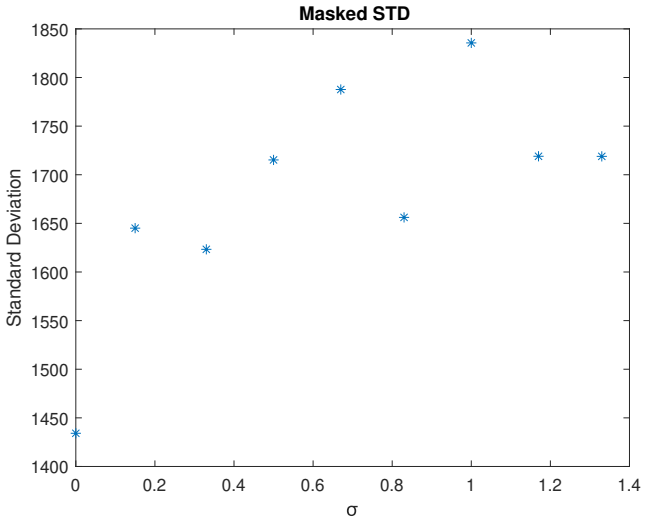

Figure 4.5: Standard deviation of the masked magnitude plot for all the experiment scans

5

Conclusion

The advancements in MRI technology have always been crucial to the evolution of medical imaging in general. As MRI advances, so does the need for more accurate, realistic, in-depth, and comprehensive models to visualize and analyze medical imaging data. This thesis explored the generalized signal model, a mathematical signal model that promises to go beyond the standard MRI model by considering scattered fields introduced by the dielectric properties of human tissue.

The research hypothesis is that the dielectric properties of a body undergoing MRI scanning, when varied, significantly affect the resulting magnetic field strength after excitation. Through S4L simulations, has been shown that altering the dielectric properties of a dielectric solution, affects the solution's ability to interact with the magnetic field and results in variations in the measured magnetic field.

The first research question is whether the dielectric properties of tissues affect the received MRI signal. As shown in the simulations, there's a high correlation between increasing the conductivity and the received signal. The exact correlation could not be derived in this research. The first reason is that a rearrangement of the generalized signal model has to be formulated to "match" the excitation sequence of the MRI. Secondly, it has been shown that not only the dielectric properties affect the measured signal but the excitation sequence too. Although this was shown in the simulation, during the experiment only one excitation sequence was used. Furthermore, research has to be made to verify empirically the latter. Although in simulations both conductivity and relative permittivity were examined, during the experiment it was hard to test the relative permittivity values as it requires an expensive chemical to be added to the dielectric solution. In regards to the experiment, the maximum values of the masked magnitude plots show that increasing the conductivity increases the receiving signal too. However, to get more confidence in those results, better simulations have to be carried out, and more than one receiving coil can be added to the setup. Furthermore due to limitations a 7T MRI machine was not available, using a higher frequency MRI machine could show the same results as in the simulations.

The second research question is how the dielectric properties alter the received signal. Simulations suggest that by increasing the conductivity, the receiving signal decreases too, which is what the generalized signal model suggests. However, the experiment didn't show the same trend. By only plotting the masked magnitude plots, there is not any significant difference in the resulting received signal. This can be explained due to various reasons. For example, the sensitivity of the coil. If the difference in the magnetic field is relatively small, this difference can not be captured by the receiving coil. Another solution is to experiment with an even higher-field MRI machine. As can be seen in the model, the higher the frequency, the higher the contributions of the dielectric properties. Furthermore, by exciting the whole ball, instead of using a beam of a single emitting loop, one can use the generalized signal model for a direct comparison. Note that, simulating the excitation of the whole sphere would be complicated.

The third question is how the beam excitation sequence affects the received signal. Due to time limitations, the experimental verification for these questions was not possible. However, it is clear in the simulations that the beam excitation sequence does affect the relation between the magnetic field strength and the conductivity. Another experiment has to be carried out to verify this hypothesis.

Furthermore, it is aimed to answer how the generalized signal model compares to the standard model. It seems that the ability of the generalized model to take into account the dielectric properties

of the tissue is crucial. Although the exact correlation between dielectric properties and the received signal was not validated, it is clear that altering conductivity alters the received signal.

The attempt to verify these results, using a 3T MRI machine, validated only to a certain extent the theoretical and simulated findings up to a point. There is a clear correlation between increasing conductivity and obtaining an altered magnetic field. This relationship between conductivity and magnetic field strength has to be further researched as it seems to have implications on MRI imaging and can potentially lead to better and more accurate imaging. As has been seen in simulations, relative permittivity also affects the resulting magnetic field strength, however, this has been outside the scope of this research. However, it is strongly recommended that this be investigated in the future. Although the simplification of the generalized signal model requires the whole ball to be excited (which was not the case for our experiment), we can still use it to explain the results of our S4L simulations and experiment results.

In conclusion, this thesis only shows the impact of conductivity and potentially relative permittivity on MRI signal models through simulations. The generalized signal model offers a promising future in MRI research and medical applications, because of its ability to account for scattered fields. As MRI technology evolves, it is important to have mathematical models that reflect real-life magnetic field interactions to explore the full potential of MRI technology and have more groundbreaking medical imaging research and technology.

References

[1] H. D. W. Hill and R. E. Richards, "Limits of measurement in magnetic resonance," Tech. Rep., 1968.

[2] P. Marzola, F. Osculati, and A. Sbarbati, "High field MRI in preclinical research," *European Journal of Radiology*, vol. 48, no. 2, pp. 165–170, Nov. 2003, ISSN: 0720-048X. DOI: 10.1016/J.EJRAD.2003.08.007.

[3] P. S. Fuchs and R. F. Remis, "Generalized Signal Models and Direct FID-Based Dielectric Parameter Retrieval in MRI," *IEEE Transactions on Antennas and Propagation*, vol. 70, no. 2, pp. 1451–1461, Feb. 2022, ISSN: 15582221. DOI: 10.1109/TAP.2021.3111324.

[4] Liang Zhi-Pei and Lauterbur Paul C., *Principles of Magnetic Resonance Imaging: A Signal Processing Perspective* | *IEEE eBooks* | *IEEE Xplore*, 2000. [Online]. Available: https://ieeexplore-ieee-org.tudelft.idm.oclc.org/book/5264284.

[5] M. E. Ladd, P. Bachert, M. Meyerspeer, *et al.*, "Pros and cons of ultra-high-field MRI/MRS for human application," *Progress in Nuclear Magnetic Resonance Spectroscopy*, vol. 109, pp. 1–50, Dec. 2018, ISSN: 00796565. DOI: 10.1016/J.PNMRS.2018.06.001.

[6] P. A. Bottomley and E. R. Andrew, "RF Magnetic Field Penetration, Phase Shift and Power Dissipation in Biological Tissue: Implications for NMR Imaging," Tech. Rep. 4, 1978, pp. 630–643.

[7] W. Schnell, "Ultimate signal-to-noise-ratio of surface and body antennas for magnetic resonance imaging," *IEEE Transactions on Antennas and Propagation*, vol. 48, no. 3, pp. 418–428, 2000, ISSN: 0018926X. DOI: 10.1109/8.841903.

[8] R. Lattanzi and D. K. Sodickson, "Ideal current patterns yielding optimal signal-to-noise ratio and specific absorption rate in magnetic resonance imaging: Computational methods and physical insights," *Magnetic Resonance in Medicine*, vol. 68, no. 1, pp. 286–304, 2012, ISSN: 15222594. DOI: 10.1002/mrm.23198.

[9] B. Guérin, J. F. Villena, A. G. Polimeridis, *et al.*, "The ultimate signal-to-noise ratio in realistic body models," *Magnetic Resonance in Medicine*, vol. 78, no. 5, pp. 1969–1980, Nov. 2017, ISSN: 15222594. DOI: 10.1002/mrm.26564.

[10] M. Cavagnaro, F. Frezza, R. Laurita, F. Mangini, and A. Palombo, "FROM MAGNETIC RESONANCE IMAGING TO DIELECTRIC PROPERTIES OF TISSUES," Tech. Rep. 2, 2011, p. 1.

[11] J L Schepps and K R Foster, "The UHF and microwave dielectric properties of normal and tumour tissues: variation in dielectric properties with tissue water content,"

[12] E. M. Haacke, L. S. Petropoulos, E. W. Nilges, and D. H. Wu, "Extraction of conductivity and permittivity using magnetic resonance imaging," *Physics in Medicine & Biology*, vol. 36, no. 6, p. 723, Jun. 1991, ISSN: 0031-9155. DOI: 10.1088/0031-9155/36/6/002. [Online]. Available: https://iopscience.iop.org/article/10.1088/0031-9155/36/6/002%20https://iopscience.iop.org/article/10.1088/0031-9155/36/6/002/meta.

[13] T. Voigt, U. Katscher, and O. Doessel, "Quantitative conductivity and permittivity imaging of the human brain using electric properties tomography," *Magnetic resonance in medicine*, vol. 66, no. 2, pp. 456–466, 2011, ISSN: 1522-2594. DOI: 10.1002/MRM.22832. [Online]. Available: https://pubmed.ncbi.nlm.nih.gov/21773985/.

[14] A. De Hoop, *Handbook of radiation and scattering of waves: Acoustic waves in fluids, elastic waves in solids, electromagnetic waves: with corrections*. Academic Press, 2008, ISBN: 0-12-208655-4. [Online]. Available: http://resolver.tudelft.nl/uuid:1a78df5c-3a7a-4b99-8f8a-5c7bc628c577.

A

Matlab Code

```
"""
clear;
close all;
clc;

%% Data
load('C:\Users\Georgios\iCloudDrive\Thesis\effect-of-dielectric\00\Grid_raw.mat')
load('C:\Users\Georgios\iCloudDrive\Thesis\effect-of-dielectric\00\H_raw.mat')
load('C:\Users\Georgios\iCloudDrive\Thesis\effect-of-dielectric\00\B_raw.mat')
Bx00= reshape(B(:,1),Grid_size);
By00= reshape(B(:,2),Grid_size);
Bz00= reshape(B(:,3),Grid_size);
load('C:\Users\Georgios\iCloudDrive\Thesis\effect-of-dielectric\01\Grid_raw.mat')
load('C:\Users\Georgios\iCloudDrive\Thesis\effect-of-dielectric\01\H_raw.mat')
load('C:\Users\Georgios\iCloudDrive\Thesis\effect-of-dielectric\01\B_raw.mat')
Bx01= reshape(B(:,1),Grid_size);
By01= reshape(B(:,2),Grid_size);
Bz01= reshape(B(:,3),Grid_size);
load('C:\Users\Georgios\iCloudDrive\Thesis\effect-of-dielectric\02\Grid_raw.mat')
load('C:\Users\Georgios\iCloudDrive\Thesis\effect-of-dielectric\02\H_raw.mat')
load('C:\Users\Georgios\iCloudDrive\Thesis\effect-of-dielectric\02\B_raw.mat')
Bx02= reshape(B(:,1),Grid_size);
By02= reshape(B(:,2),Grid_size);
Bz02= reshape(B(:,3),Grid_size);
load('C:\Users\Georgios\iCloudDrive\Thesis\effect-of-dielectric\03\Grid_raw.mat')
load('C:\Users\Georgios\iCloudDrive\Thesis\effect-of-dielectric\03\H_raw.mat')
load('C:\Users\Georgios\iCloudDrive\Thesis\effect-of-dielectric\03\B_raw.mat')
Bx03= reshape(B(:,1),Grid_size);
By03= reshape(B(:,2),Grid_size);
Bz03= reshape(B(:,3),Grid_size);
load('C:\Users\Georgios\iCloudDrive\Thesis\effect-of-dielectric\04\Grid_raw.mat')
load('C:\Users\Georgios\iCloudDrive\Thesis\effect-of-dielectric\04\H_raw.mat')
load('C:\Users\Georgios\iCloudDrive\Thesis\effect-of-dielectric\04\B_raw.mat')
Bx04= reshape(B(:,1),Grid_size);
By04= reshape(B(:,2),Grid_size);
Bz04= reshape(B(:,3),Grid_size);
load('C:\Users\Georgios\iCloudDrive\Thesis\effect-of-dielectric\05\Grid_raw.mat')
load('C:\Users\Georgios\iCloudDrive\Thesis\effect-of-dielectric\05\H_raw.mat')
load('C:\Users\Georgios\iCloudDrive\Thesis\effect-of-dielectric\05\B_raw.mat')
Bx05= reshape(B(:,1),Grid_size);
By05= reshape(B(:,2),Grid_size);
Bz05= reshape(B(:,3),Grid_size);
load('C:\Users\Georgios\iCloudDrive\Thesis\effect-of-dielectric\06\Grid_raw.mat')
load('C:\Users\Georgios\iCloudDrive\Thesis\effect-of-dielectric\06\H_raw.mat')
load('C:\Users\Georgios\iCloudDrive\Thesis\effect-of-dielectric\06\B_raw.mat')
Bx06= reshape(B(:,1),Grid_size);
By06= reshape(B(:,2),Grid_size);
Bz06= reshape(B(:,3),Grid_size);
load('C:\Users\Georgios\iCloudDrive\Thesis\effect-of-dielectric\07\Grid_raw.mat')
load('C:\Users\Georgios\iCloudDrive\Thesis\effect-of-dielectric\07\H_raw.mat')
```

```
load('C:\Users\Georgios\iCloudDrive\Thesis\effect-of-dielectric\07\B_raw.mat')
Bx07= reshape(B(:,1),Grid_size);
By07= reshape(B(:,2),Grid_size);
Bz07= reshape(B(:,3),Grid_size);
load('C:\Users\Georgios\iCloudDrive\Thesis\effect-of-dielectric\08\Grid_raw.mat')
load('C:\Users\Georgios\iCloudDrive\Thesis\effect-of-dielectric\08\H_raw.mat')
load('C:\Users\Georgios\iCloudDrive\Thesis\effect-of-dielectric\08\B_raw.mat')
Bx08= reshape(B(:,1),Grid_size);
By08= reshape(B(:,2),Grid_size);
Bz08= reshape(B(:,3),Grid_size);


%%

for i=1:length(ZAxis)-1
    len_z(i)= (ZAxis(i)-ZAxis(i+1));
    z_points(i) =  (ZAxis(i)+ZAxis(i+1))/2;
end

for i=1:length(YAxis)-1
    len_y(i)= (YAxis(i)-YAxis(i+1));
    y_points(i) =  (YAxis(i)+YAxis(i+1))/2;
end

for i=1:length(XAxis)-1
    len_x(i)= (XAxis(i)-XAxis(i+1));
    x_points(i) =  (XAxis(i)+XAxis(i+1))/2;
end

%%
omega =2*pi*298*10^(6);
mu0= 1.2566*10^(-6);
e0= 8.8541878128*10^(-12) ;
c= 1/sqrt(e0*mu0);
gamma = (1i*omega)/c;

V_temp_z = zeros(9,1);

for z_receiver=36 %z= ~0mm
    for i=1:length(XAxis)-1
        x_ind = x_points(i);
        for j=1:length(YAxis)-1
             y_ind = y_points(j);
            if ( (i>48 && i<52) && (j>211 && j<215)) %SQUARE
                area_of_cell = abs(len_x(i)*len_y(j));
                %area_of_cell = 1;
                V_temp_z(:,1) = [area_of_cell*Bz00(i,j,z_receiver)+V_temp_z(1,1);area_of_cell
                    *Bz01(i,j,z_receiver)+V_temp_z(2,1);area_of_cell*Bz02(i,j,z_receiver)+
                    V_temp_z(3,1);area_of_cell*Bz03(i,j,z_receiver)+V_temp_z(4,1);
                    area_of_cell*Bz04(i,j,z_receiver)+V_temp_z(5,1);area_of_cell*Bz05(i,j,
                    z_receiver)+V_temp_z(6,1);area_of_cell*Bz06(i,j,z_receiver)+V_temp_z(7,1)
                    ;area_of_cell*Bz07(i,j,z_receiver)+V_temp_z(8,1);area_of_cell*Bz08(i,j,
                    z_receiver)+V_temp_z(9,1)];
            end
        end
    end
end
% V_temp_y = zeros(9,1);
% for y_receiver=62 %y=56mm
%     for i=1:length(XAxis)-1
%         x_ind = x_points(i);
%         for j=1:length(ZAxis)-1
%              z_ind = z_points(j);
%              if ( (abs(x_ind)< 0.2) && (abs(z_ind)< 0.2) ) %SQUARE
%                 V_temp_y(:,1) = [By00(i,y_receiver,j)+V_temp_y(1,1);By01(i,y_receiver,j)+
    V_temp_y(2,1);By02(i,y_receiver,j)+V_temp_y(3,1);By03(i,y_receiver,j)+V_temp_y(4,1);By04(
    i,y_receiver,j)+V_temp_y(5,1);By05(i,y_receiver,j)+V_temp_y(6,1);By06(i,y_receiver,j)+
    V_temp_y(7,1);By07(i,y_receiver,j)+V_temp_y(8,1);By08(i,y_receiver,j)+V_temp_y(9,1)];
%              end
%         end
%     end
```

```
% end

V_z = (1i*omega)*V_temp_z;
% V_y = (1i*omega)*V_temp_y;
sigma=[0;0.1;0.2;0.3;0.4;0.5;0.6;0.7;0.8];

figure()
plot(sigma,abs(V_z),"*")
title("Induced Voltage, at z=55m")
ylabel("Induced Voltage")
xlabel (" [S/m]")

% figure()
% plot(sigma,abs(V_y),"*")
% title("Induced Voltage, at y=55m")
% ylabel("Induced Voltage")
% xlabel (" [S/m]")

max_lim=2E-15;
min_lim = 0;


figure()
imagesc(x_points,y_points,squeeze(abs(Bz03(48:end,:,116)))'-squeeze(abs(Bz00(48:end,:,116)))
    ',[min_lim max_lim])
colorbar
xlabel("x-axis")
ylabel("y-axis")
title ("=0.3 z=0 m, z-component")

figure()
imagesc(x_points,y_points,squeeze(abs(Bz01(48:end,:,116)))'-squeeze(abs(Bz00(48:end,:,116)))
    ',[min_lim max_lim])
colorbar()
xlabel("x-axis")
ylabel("y-axis")
title ("=0.1 z=0.0 m, z-component")

figure()
imagesc(x_points,y_points,squeeze(abs(Bz00(48:end,:,116)))',[min_lim max_lim])
colorbar
xlabel("x-axis")
ylabel("y-axis")
title ("=0.0 z=0.0 m, z-component")


figure()
imagesc(x_points,y_points,squeeze(abs(Bz02(48:end,:,116)))'-squeeze(abs(Bz00(48:end,:,116)))
    ',[min_lim max_lim])
colorbar
xlabel("x-axis")
ylabel("y-axis")
title ("=0.2 z=0.0 m, z-component")

% figure()
% imagesc(x_points,z_points,squeeze(abs(By05(47:end,61,:)))',[min_lim max_lim])
% colorbar
% xlabel("x-axis")
% ylabel("y-axis")
% title(" y=0.056 m, y-component")
```